



**HAL**  
open science

## Field biotite weathering rate determination using U-series disequilibria

Sophie Rihs, Adrien Gontier, Alexandre Voinot, François Chabaux, Eric Pelt,  
Damien Lemarchand, Marie-Pierre Turpault

► **To cite this version:**

Sophie Rihs, Adrien Gontier, Alexandre Voinot, François Chabaux, Eric Pelt, et al.. Field biotite weathering rate determination using U-series disequilibria. *Geochimica et Cosmochimica Acta*, 2020, 276, pp.404 - 420. 10.1016/j.gca.2020.01.023 . hal-03490193

**HAL Id: hal-03490193**

**<https://hal.science/hal-03490193>**

Submitted on 20 May 2022

**HAL** is a multi-disciplinary open access archive for the deposit and dissemination of scientific research documents, whether they are published or not. The documents may come from teaching and research institutions in France or abroad, or from public or private research centers.

L'archive ouverte pluridisciplinaire **HAL**, est destinée au dépôt et à la diffusion de documents scientifiques de niveau recherche, publiés ou non, émanant des établissements d'enseignement et de recherche français ou étrangers, des laboratoires publics ou privés.



Distributed under a Creative Commons Attribution - NonCommercial 4.0 International License

## Field biotite weathering rate determination using U-series disequilibria

RIHS Sophie<sup>a\*§</sup>, GONTIER Adrien<sup>a\*</sup>,

VOINOT Alexandre<sup>a,§</sup>, CHABAUX François<sup>a</sup>, PELT Eric<sup>a</sup>, LEMARCHAND Damien<sup>a</sup>, TURPAULT Marie-Pierre<sup>b</sup>

<sup>a</sup> Laboratoire d'Hydrologie et de Géochimie de Strasbourg, EOST, Université de Strasbourg and CNRS, 1 rue Blessig, 67084 Strasbourg cedex, France.

<sup>b</sup> Laboratoire de Biogéochimie des Ecosystèmes Forestiers, INRA, Champenoux, France

§ present address: Queen's Facility for Isotope Research, Department of Geological Sciences and Geological Engineering, Miller Hall, 36 Union St, K7L3N6 Kingston, Ontario, Canada

\* Equal contribution from the first two authors.

§ Corresponding author: [rihs@unistra.fr](mailto:rihs@unistra.fr)

# 1 **Abstract**

2 The chemical weathering rate of silicates is a key parameter of several geochemical  
3 processes; however, the long-term field measurement of these rates remains challenging.  
4 Currently, there are several methods for quantifying field weathering rates, but each  
5 presents its own unique set of difficulties. In this study uranium-series nuclides were used to  
6 investigate long-term biotite weathering in a soil profile. For this purpose, pseudomorph  
7 grains of biotites (including weathering products) were hand-picked from four horizons of a  
8 soil profile and from underlying granitic saprolite from the experimental Breuil-Chenue site  
9 (France).

10 Unexpected behaviors of U and Th nuclides were recorded from these samples. An  
11 unambiguous leaching of  $^{232}\text{Th}$  occurs during the weathering of biotite, while reduced U  
12 release relative to Th was observed, implying an efficient redistribution of U between the  
13 primary mineral and weathering products within the pseudomorphs. The measured U-series  
14 activity ratios reflect a regular and self-consistent pattern evolution. However, the "U-series-  
15 derived-weathered-stage" is not always coherent with the weathering features of major  
16 elements and/or with the location of the samples within the soil profile. For instance, biotite  
17 from the saprolite displays U-series activity ratios typical of significantly weathered samples,  
18 while major elements present rather limited signs of weathering. These results suggest an  
19 incongruent leaching of U and Th isotopes and suggest that U- and Th-series nuclides probe  
20 some water-mineral interactions that occur before macroscopic mineral transformation.

21 Using an open-system leaching model, coupled ( $^{234}\text{U}/^{238}\text{U}$ ), ( $^{234}\text{U}/^{230}\text{Th}$ ), and ( $^{226}\text{Ra}/^{230}\text{Th}$ )  
22 disequilibria measured from the samples allow us to calculate a weathering duration range  
23 of 6 to 52 ka for most weathered samples of this soil profile. The biotite weathering rate  
24 deduced from these data ranges from  $7.8 \times 10^{-17} \text{ mol.m}^{-2}.\text{s}^{-1}$  to  $6.5 \times 10^{-16} \text{ mol.m}^{-2}.\text{s}^{-1}$ , which is  
25 consistent with the range of field rates previously reported. This rate was compared to the  
26 weathering rate of biotites induced by the substitution of vegetation occurring 35 years ago  
27 in a nearby soil profile, which was about 2 - 3 orders of magnitude higher than the long-term  
28 rate reported above. This feature is perfectly consistent with the decrease in the weathering  
29 rate with time that was previously widely documented but that still remains debated. Our  
30 results allude to a valuable use of U-series isotopes for mineral-weathering field rate  
31 determination and report a decrease in silicate weathering rates over long- (10 000s of

32 years) and short-term (10s of years) weathering events recorded from the same site. The  
33 results show that short term laboratory experiments can be representative of field  
34 processes, and suggest that some forms of mineral weathering reactivation, similar to that  
35 observed during laboratory experiments, may naturally occur in soils in response to high  
36 frequency perturbation processes such as land cover change.

37

38 **Keywords:** biotite, field weathering rate, U-series

39

## 40 **1. Introduction**

41 Concerns regarding climate change and soils sustainability have urged scientists to better  
42 understand rates of weathering. Indeed, such chemical reactions can regulate atmospheric  
43 CO<sub>2</sub> concentration (Berner et al., 1997; Gaillardet et al., 1999) or neutralize acid rain (Drever  
44 and Hurcomb, 1986) through the consumption of carbon and/or protons. They can also  
45 affect soil fertility. For instance, mica weathering has been intensively studied, as mica is a  
46 source of nutrients essential for plant growth, including potassium, magnesium and iron  
47 (Hinsinger et al., 1992; Leyval et al., 1991; Martin et al., 2010; Turpault and Trotignon, 1994).  
48 Over recent decades, numerous studies have focused on determining mineral weathering  
49 rates through either short-term laboratory experiments or long-term field studies. These  
50 studies clearly demonstrate the time dependence of the weathering rate, with short-term  
51 laboratory rates generally being several orders of magnitude faster than long-term rates  
52 (Taylor and Blum, 1995; White et al., 2003; Maher et al., 2004; White and Buss, 2014, Buss et  
53 al., 2017). The cause of this discrepancy remains highly debated (e.g., Hochella and Banfield,  
54 1995; Maher et al., 2006a, 2009; Hellman et al., 2012; White et al., 2017). One of the  
55 difficulties associated with this puzzle may arise from the reduced value and precision of  
56 long term rate determination, which relies on dissolved fluxes being exported by rivers  
57 and/or aquifers (e.g., Clow and Drever, 1996) or on change in regolith composition (e.g.,  
58 White, 2002), implying the deconvolution of a specific mineral weathering among several  
59 others. A lack of "mid-term" data, i.e., on the 10s or 100s of years scale, also prevents the  
60 precise determination of the time dependency of the weathering rate equation, which  
61 would heavily constrain kinetic and therefore involved mechanisms.

62 U-series nuclides have previously been used to determine weathering rates in regoliths and  
63 soils over various time scales (Chabaux et al., 2003a, 2003b, 2013; Dequincey et al., 2002;  
64 Dosseto et al., 2008, 2012; Keech et al., 2013; Ma et al., 2010, 2012, 2013; Pelt et al., 2008;  
65 Rihs et al., 2011; Suresh et al., 2013, Gontier et al., 2015; Ackerer et al., 2016; Schoonejans  
66 et al., 2016 , see also Chabaux et al. (2008), and Vigier and Bourdon (2011) for recent  
67 reviews). The use of these nuclides as weathering chronometers is based on chemical and  
68 physical fractionation that occurs between a parent and its daughter nuclides during  
69 weathering processes, leading to a radioactive disequilibrium. The evolution of the  
70 weathered material composition during weathering is therefore modeled as the continuous

71 loss and gain of nuclides (precipitation/adsorption from atmospheric deposition and/or  
72 illuviation) in addition to radioactive decay. According to this open model, the disequilibrium  
73 between U-series nuclides evolves over time until a steady state is reached. The amount of  
74 time required to reach this steady state depends on the ratio between the various input,  
75 leaching and radioactive decay rates. During this period, the extent of U-series disequilibria  
76 records the amount of time elapsed since the inception of the loss and/or gain process, i.e.,  
77 the inception of parent material weathering. The matching of the half-lives of U- and Th-  
78 series nuclides, i.e., 5 y to 247 ky, and the timescales of pedogenic and weathering processes  
79 render these nuclides particularly suitable for inferring the time constants of element  
80 transfers within soils or saprolite layers. Dosseto et al. (2014) used the U-series derived  
81 weathering ages of bulk sediments to indirectly determine catchment-wide mineral-specific  
82 weathering rates. Even more recently, Dosseto et al. (2019) investigated the use of  
83 separated biotite and quartz to infer the mineral dissolution rates as well as the regolith  
84 production rate. Except this recent study, the potential for U-series to determine the long-  
85 term weathering rate of a specific mineral remains largely unexplored.

86 In the present work, we investigate a new application of U series chronometer to ascertain  
87 the long-term biotite weathering rate within a soil profile. Biotite was chosen among  
88 common other silicate minerals in view of its generally high U concentration. For this  
89 purpose, U- series disequilibria were measured in several biotite grains extracted from a  
90 granitic soil profile previously studied at the bulk scale.

91

## 92 **2. Material and methods**

### 93 **2.1 Site location**

94 Sand-sized biotite grains were sampled from a soil profile located in the Breuil-Chenue forest  
95 (Morvan Mountains, 47°18'N-4°5'E, 638 m, France) (Fig. 1). This experimental site was  
96 established by the Institut National de Recherche Agronomique (INRA) in 1976 and belongs  
97 to the SOERE FORET and ANAEE network ([www.gip-ecofor.org/f-ore-t/reseau](http://www.gip-ecofor.org/f-ore-t/reseau)). Mean annual  
98 air temperature and precipitation levels are 9 °C and 1280 mm respectively (Calvaruso et al.,  
99 2009). The native vegetation is composed of 150-year-old forest dominated by beech trees  
100 (*Fagus sylvatica* L). The bedrock is composed of coarsely grained facies of "Pierre qui Vire"  
101 leucogranite (Seddoh, 1973) with a mineralogical composition of 34 % quartz, 24 % K-

102 feldspar, 31 % albite, 9 % muscovite, 1.2 % biotite, 0.5 % chlorite and accessory minerals  
103 (Mareschal et al., 2015). Soils that have developed over this bedrock are acidic (pH range:  
104 4.17-4.96, Rihs et al., 2016), well drained, and classified as Typic Dystrochrept with depths  
105 ranging from 120 to 140 cm. Mineralogical and physico- chemical descriptions can be found  
106 in Mareschal (2008), Mareschal et al. (2010; 2015) and Gontier et al. (2015). It should be  
107 noted that some residual gravels (grain size > 2 mm) of granite are still present throughout  
108 the entire soil profile (from 17 to 31 %<sub>w</sub>t in the different soil layers, Mareschal, 2008). The  
109 late breakdown of the residual granite block can therefore release fresh biotite grains to the  
110 shallow soil layers. Two major forms of ongoing mineralogical transformation were  
111 identified: i) close to the bedrock, biotite and albite are transformed into kaolinite and  
112 gibbsite, and ii) in the surface layers, remaining biotite and muscovite are transformed into  
113 vermiculite and smectite with the precipitation of aluminum hydroxides in their interlayer  
114 sheets (Mareschal, 2008).

115

## 116 **2.2 Mineral separation and treatments**

117 Biotite grains were extracted from the following soil layers: 20-30 cm, 110-120 cm, 120-130  
118 cm and 120-140 cm throughout a joint study (Voinot 2012). Aliquots of the same samples  
119 (except for the 120-140 cm sample) were analyzed in both studies. The grains were manually  
120 hand-picked from the bulk soil, except for the 20-30 cm horizon, from which biotite grains  
121 were extracted from the 50 - 200 µm and 0.2 - 2 mm soil fractions. Additional magnetic  
122 separation was performed using a magnetic sector and vibrator (AA DYNA-MITE Electric  
123 vibrator 230V 50Hz, 10VA). No heavy liquid was used during separation to avoid any  
124 contamination and/or leaching of the samples. Approximately 100 mg to 1 g of mineral was  
125 collected from each soil layer before being manually crushed in an agate mortar.

126 Biotite grains taken from a block of the granite sampled from saprolite at the bottom of the  
127 soil profile were also analyzed (corresponding to sample B<sub>0b</sub> in Voinot 2012). The samples  
128 were recovered after crushing a macroscopically unaltered granite block. Two aliquots of the  
129 extracted grains were sampled for replicate analyses. In addition, this sample was treated to  
130 extract its interlayer and weakly bounded nuclides. The interlayer was extracted from  
131 roughly 50 mg of the sample with 40 ml of 1 M NaCl (pH 5.50) heated at 80°C over 7 days.  
132 After centrifugation, the supernatant was collected and acidified at pH < 2 before analysis.  
133 Fresh NaCl solution was added to the residual solid and extraction was repeated two more

134 times. U and Th concentrations were measured from the 3 sequentially extracted solutions.  
135 Major elements in the final residual solid treated with NaCl were analyzed after rinsing them  
136 with MilliQ water. Approximately 40 mg of this sample was also treated with 40 ml of a 0.2  
137 M oxalate acid/ ammonium oxalate solution ( $C_2O_4H_2, 2H_2O - (NH_4)_2C_2O_4, H_2O$ ) at pH 3  
138 (Tamm, 1922, modified by Schwertmann, 1964). The purpose of this treatment was to  
139 extract amorphous and poorly crystallized Fe-Mn-Al oxy-hydroxides in addition to the sorbed  
140 fraction. The suspension was shaken over 4 hours in the dark, before being centrifuged at  
141 5000 rpm for 5 min. The supernatant was collected for U, Th and Mg analyses.

142

### 143 **2.3 Analytical techniques**

144  $^{238}U$ ,  $^{232}Th$  and  $^{226}Ra$  contents were determined by isotope dilution along with U-Th isotopic  
145 compositions of the same powder digestion. Between 5 and 10 mg of the powdered samples  
146 were spiked with a purified  $^{228}Ra$  and artificial  $^{233}U$ - $^{229}Th$  tracers calibrated with AThO rock -  
147 standard (Williams et al., 1992, Condomines et al., 1995). The dissolution procedure involved  
148 digestion in a distilled  $HNO_3$ -HF-  $HClO_4$  acids mixture at 70°C before subsequent evaporation.  
149 The residues were then dissolved with HCl- $H_3BO_3$  acids at 100°C for 24 h, prior to  
150 subsequent evaporation. U-Th separation and purification procedures were carried out using  
151 the anion exchange chromatography techniques developed at the Laboratory of Hydrology  
152 and Geochemistry of Strasbourg (LHyGeS) (Dequincey et al., 2002; Granet et al., 2007; Pelt et  
153 al., 2008). Ra separation and purification were performed following the procedure  
154 developed by Pelt et al. (2013) and adapted from previous works by Chabaux et al. (1994)  
155 and Ghaleb et al. (2004).

156 Th concentrations and  $^{232}Th/^{230}Th$  isotopic ratios were measured with a Thermo-  
157 Scientific Neptune multiple collector inductively coupled plasma mass spectrometer (MC-  
158 ICP-MS). Thorium concentrations were calculated from the measured  $^{232}Th/^{229}Th$  ratios. A  
159 standard-sample-standard bracketing method was applied to correct raw data for  
160 instrumental mass bias using a mixture of IRMM035 standard solution and  $^{229}Th$  spike (see  
161 Jeanbrun et al., 2012 for details). The  $^{232}Th/^{230}Th$  isotopic ratio proposed by Sims et al.  
162 (2008) for the IRMM-035 standard was used ( $87873 \pm 738$  2SD) rather than the original  
163 certified value. The abundance sensitivity at 2 amu was ~30 ppb with an ~70-80 %  
164 transmission of the RPQ filter and yielded to  $^{232}Th$  tailing on the  $^{230}Th$  that was always valued

165 at less than 0.5 %. Therefore, no corrections were made for this negligible shift covered by  
166 analytical uncertainties.

167 The U and  $^{226}\text{Ra}$  concentrations and  $^{234}\text{U}/^{238}\text{U}$  isotopic ratios were measured by thermal  
168 ionization mass spectrometry (TIMS) using a Thermo- Scientific Triton mass spectrometer.  
169 The U concentrations were calculated from the measured  $^{233}\text{U}/^{235}\text{U}$  ratios. The  $^{226}\text{Ra}$   
170 concentrations were calculated from the measured  $^{226}\text{Ra}/^{228}\text{Ra}$  spiked ratios and the natural  
171  $^{226}\text{Ra}/^{228}\text{Ra}$  ratio estimated from the  $^{230}\text{Th}/^{232}\text{Th}$  isotopic ratio assuming a radioactive  
172 equilibrium between  $^{232}\text{Th}$  and  $^{228}\text{Ra}$  activity, i.e.,  $(^{228}\text{Ra}) = (^{232}\text{Th})$ . Due to the low percentage  
173 of  $^{228}\text{Ra}$  arising from the sample in the sample-spike mixture (< 1 %), a shift from this  
174 assumed radioactive equilibrium would produce a negligible effect on the calculated  $^{226}\text{Ra}$   
175 concentration (e.g., less than 0.1 % for a 10 % shift away from the radioactive  $^{232}\text{Th} - ^{228}\text{Ra}$   
176 equilibrium).

177 Measurement accuracy and reproducibility were controlled by analyzing the HU1  
178 uranium and IRMM-036 thorium standard solutions, the BE-N and BCR-2 rock- standards,  
179 and the isotopic ratio of the Ra spike measured before each sample series. The change in the  
180 Ra spike isotopic ratio observed over time due to  $^{228}\text{Ra}$  decay was found to be consistent  
181 with theoretical decay within 0.6 % (2SD, N=19, 2012). Average ( $^{234}\text{U}/^{238}\text{U}$ ) activity ratios and  
182  $^{232}\text{Th}/^{230}\text{Th}$  isotopic ratios measured in the HU1 and IRMM-036 standards were equal to  
183  $1.000 \pm 0.007$  (2 SD, N=24, 2012-2013) and  $325,261 \pm 2664$  (2 SD, N=9, 2012), respectively, in  
184 agreement with previously published values for HU1 (Cheng et al., 2000; Delanghe et al.,  
185 2002) and IRMM-036 (Sims et al., 2008; Ma et al., 2012). Replicate analyses of BE-N and BCR-  
186 2 rock standards are reported in Table 1. These analyses yielded analytical uncertainty values  
187 (2SD, N = 9, 2012-2014) of 1 % for U and Th concentrations, of 1.5 % for  $^{226}\text{Ra}$   
188 concentrations, of less than 0.5 % for ( $^{234}\text{U}/^{238}\text{U}$ ) ratios, of 1% for ( $^{230}\text{Th}/^{232}\text{Th}$ ) ratios, of 1.5  
189 % for ( $^{230}\text{Th}/^{234}\text{U}$ ) ratios and of 2 % for ( $^{226}\text{Ra}/^{230}\text{Th}$ ) ratios, in agreement with previously  
190 published values for BE-N (Govindaraju, 1994; Pelt et al., 2013; Carpentier et al., 2016) and  
191 BCR-2 (Sims et al., 2008; Koornneef et al., 2010; Carpentier et al., 2016; Cogez et al., 2018).  
192 The results highlight a slight  $\sim 7$  ‰ enrichment in  $^{230}\text{Th}$  compared to secular equilibrium and  
193 compared to data from Sims et al. (2008) and Carpentier et al. (2016), most probably related  
194 to the lack of  $^{232}\text{Th}$  tailing correction before 2014 and to the uncertainty assigned to the  
195 IRMM035 bracketing standard. Total process blanks ranged from 60 to 120 pg for Th, ranged

196 from 2 to 90 pg for U and were valued at less than 0.05 fg for <sup>226</sup>Ra, thus representing less  
197 than 1 ‰ of the analyzed samples.

198

199 Major elements in the mineral after interlayer extraction and Mg content in the oxalate  
200 solution were measured by Inductively Coupled Plasma Atomic Emission Spectrometry (ICP-  
201 AES) while U and Th concentrations in the extracted solutions were determined by  
202 Inductively Coupled Plasma Mass Spectrometry (ICP-MS). The precision and accuracy of the  
203 measured concentrations were tested by replicate analyses after alkali fusion with Li<sub>2</sub>B<sub>4</sub>O<sub>7</sub> of  
204 the basalt BE-N, anorthosite AN-G, granite GS-N, dolerite WS-E, and diorite DR-N rock  
205 standards (Govindaraju, 1994), yielding analytical uncertainties of 3 % and 10 % (2SD, N= 20  
206 for each standard over the study period) for major and trace elements, respectively.

207

208 The N<sub>2</sub>-BET specific surface area of the saprolite biotite sample of 6.0 ± 0.7 m<sup>2</sup>/g, was  
209 measured at the LIEC (Laboratoire Interdisciplinaire des Environnements Continentaux) in  
210 Nancy, France, using a BEL Japan BELSORP-mini II instrument with nitrogen (purity > 99.995  
211 %) as the adsorptive at 77 K.

212

### 213 **3. Results**

214 Previous analyses of the separated grains conducted by X-Ray diffraction and Scanning  
215 Electron Microscopy reveal that these samples do not comprise pure biotite minerals alone  
216 (Mareschal, 2008; Voinot, 2012). Mareschal (2008) studied several soil profiles from the  
217 same site and highlighted the common presence of kaolinite, vermiculite and Fe-oxides in  
218 biotite grains found in these soils. The presence of these weathering products is consistent  
219 with a decrease in SiO<sub>2</sub>/Al<sub>2</sub>O<sub>3</sub> and K<sub>2</sub>O/Al<sub>2</sub>O<sub>3</sub> ratios observed from the deepest horizons to  
220 the surface in the studied samples (Table 2). Mareschal (2008) also performed in- situ  
221 microprobe measurements of sand-size biotite grains collected from the same site and  
222 observed a decrease in the SiO<sub>2</sub> /Al<sub>2</sub>O<sub>3</sub> ratio from pristine biotite (SiO<sub>2</sub> /Al<sub>2</sub>O<sub>3</sub> = 1.8) to the  
223 weathered area (SiO<sub>2</sub> /Al<sub>2</sub>O<sub>3</sub> = 1.1) within the grains, corresponding to a kaolinization  
224 process. In addition, a decline of K<sub>2</sub>O content was observed, consistent with the widely  
225 reported release of K during biotite weathering (e.g., Newman and Brown, 1966; Newman,  
226 1969; Turpault et al. 1994; White 2002). Mareschal (2008) proposes that the weathering

227 products formed from an intragrain reprecipitation of the leached elements from weathered  
228 biotite. The separated grains therefore correspond to the pseudomorphosis of parent  
229 biotites, including weathering products retained within the unchanged volume and fabric of  
230 the parent minerals. Such pseudomorphic replacement of biotites by kaolinite has been  
231 previously well documented (e.g., White et al., 1998; 2002). The quantitative mineralogy,  
232 i.e., the mass fraction determination of each component in the grains, was quantified by  
233 Voinot (2012) through chemical analyses of the grains (reported in Table 2), differential  
234 thermal analyses, chemical analysis of each mineral and of XRD data following the  
235 methodology developed by Fichter et al. (1998) and Turpault et al. (1998). Normative  
236 calculations using standard minerals allow to determine the fraction of each mineral by  
237 resolving a system of simultaneous linear equations based on the chemical content of a  
238 particle size fraction on one hand and from the corresponding element content of single  
239 minerals on the other. Between 7 and 17 % of quartz was identified in the analyzed grains,  
240 representing an imperfect biotite grain separation. Scanning Electron Microscopy also  
241 reveals some traces of accessory minerals such as Ti oxides (< 2 %) and chlorite (< 1 %)  
242 (Voinot, 2012). In view of the low abundance of these accessory minerals or of the low U  
243 concentrations generally observed in quartz (0.1 - 1 ppm, Bosia et al., 2018; Dosseto et al.,  
244 2019), these impurities are not expected to significantly impact U-series activity ratios  
245 measured in the separated grains, wherein measured U concentrations range from 31 to 65  
246 ppm. With a view to consider the amount of weathered biotite present within the analyzed  
247 grains, the proportion of remaining biotite and the weathering products were therefore  
248 recalculated from the results of Voinot (2012) without quartz contribution, i.e.: biotite and  
249 weathering products proportions were normalized to 100 % after subtracting quartz  
250 proportion. According to this calculation, samples collected from deep soil layers are  
251 composed of about 60 % biotite (quartz excepted) while fine grains from the surface soil  
252 layer (20-30 cm 50-200  $\mu\text{m}$ ) do not hold more than 28 % (quartz excepted) of biotite  
253 anymore (Fig. 2). Consistent with the decline of  $\text{K}_2\text{O}$  content mentioned above, the  
254 remaining amount of biotite calculated strongly correlates with the  $\text{K}_2\text{O}$  concentrations and  
255 K/Fe, K/Al or Si/Al ratios (not shown). All of these parameters therefore represent equivalent  
256 proxies for the weathering state of biotite grains.

257

### 258 **3.1. U-series disequilibria**

259 U, Th concentrations and activity ratios are reported in Table 3. Replicate analyses of biotite  
260 grains from the granitic saprolite show different U and Th concentrations (differences of 5 %  
261 and 10 %, respectively while analytical uncertainties are 1 %). These replicated analyses  
262 were not performed on aliquots of a single powder sample, but on aliquots of non-crushed  
263 biotite grains, and they therefore highlight the heterogeneity of U and Th concentrations in  
264 these minerals. However, ( $^{234}\text{U}/^{238}\text{U}$ ), ( $^{230}\text{Th}/^{234}\text{U}$ ) and ( $^{226}\text{Ra}/^{230}\text{Th}$ ) activity ratios of the two  
265 subsamples are identical within analytical uncertainty, emphasizing the significance of the  
266 measured U-series disequilibria independent of probable initial U heterogeneity.

267 During water-rock interactions and therefore weathering processes, U-series nuclides are  
268 expected to fractionate. Detailed reviews can be found in Chabaux et al. (2008), or Vigier  
269 and Bourdon (2011). In brief, in an oxic environment, U is usually highly mobile while Th is  
270 known to be very insoluble. The mobility of Ra is strongly controlled by redox state but is  
271 generally higher than that of Th. In addition, fractionation between  $^{234}\text{U}$  and  $^{238}\text{U}$  isotopes  
272 may occur due to alpha-recoil process (Kigoshi, 1971). Therefore, the following features are  
273 anticipated during weathering process: U and Ra loss, Th immobility, ( $^{234}\text{U}/^{238}\text{U}$ ) and  
274 ( $^{226}\text{Ra}/^{230}\text{Th}$ ) ratio decline concomitant with an increase in the ( $^{230}\text{Th}/^{234}\text{U}$ ) ratio. In the study  
275 biotite grains, U and Th concentrations cover a broad range through the profile (30 to 65  
276 ppm and 100 to 338 ppm respectively). In the shallowest horizon (20-30 cm), concentrations  
277 in the coarse-size fraction ( $> 200 \mu\text{m}$ ) are significantly higher than those in the fine-size  
278 fraction (50- 200  $\mu\text{m}$ ). U contents do not show a clear trend with the decrease in K content  
279 while Th contents decrease significantly (Fig. 3). Consequently, the evolution of the U/Th  
280 ratio is not correlated with weathering pattern determined from major elements and  
281 mineralogy (Fig. 4a). This ratio is, in contrast, strongly correlated with Ti content (Fig. 4b).

282 ( $^{234}\text{U}/^{238}\text{U}$ ), ( $^{230}\text{Th}/^{234}\text{U}$ ) and ( $^{226}\text{Ra}/^{230}\text{Th}$ ) activity ratios range from 0.73- 0.93, from 1.04 –  
283 1.14 and from 0.67 – 0.91, respectively (Table 3). Despite an overall increase in the  
284 disequilibrium extent observed toward the surface, i.e., the deepest soil samples are closer  
285 to the secular equilibrium than samples from the topsoil layer, grains extracted from the  
286 granitic saprolite are inconsistent with this pattern of evolution, as they exhibit some of the  
287 largest disequilibria values ( $(^{234}\text{U}/^{238}\text{U}) = 0.76$ ,  $(^{230}\text{Th}/^{234}\text{U}) = 1.10$  and  $(^{226}\text{Ra}/^{230}\text{Th}) = 0.76$ ).  
288 Similarly, the two samples separated from the same topsoil layer (20-30 cm) show  
289 contrasting disequilibria ( $(^{234}\text{U}/^{238}\text{U}) = 0.73$  and 0.79 in fine  $< 200 \mu\text{m}$  and coarse  $> 200 \mu\text{m}$   
290 fractions, respectively), highlighting the size-dependence of U-series disequilibria and

291 weathering states. Such an irregular evolution of sample compositions with depth was also  
292 noticeable from the quantitative mineralogy of grains (Fig. 2). For instance, the amount of  
293 remaining biotite is significantly higher in the shallow coarse sample (20-30 cm > 200  $\mu\text{m}$ )  
294 than in samples from the deepest soil layers. In granitic weathering profiles, such inversion  
295 of weathering polarity can be easily explained. Indeed in arenas the large-scale view of  
296 upward vertical polarity observed from fresh rock to the topsoil can be disturbed at the  
297 outcrop scale through the preferential weathering of fractured zones (Meunier, 2005). In  
298 addition, the remanence of large granite gravel throughout the entire soil profile implies the  
299 release of relatively fresh (or at least less weathered) minerals in the surface soil layers. The  
300 coarse > 200  $\mu\text{m}$  sample from the 20-30 cm layer may reflect such origin while the fine < 200  
301  $\mu\text{m}$  (more weathered) fraction may have been inherited from the deeper granitic bedrock  
302 weathering front. According to this assumption, fine and coarse fractions of the 20-30 cm  
303 soil layer may therefore simply reflect different weathering durations. This implies that any  
304 time determination made for these samples cannot be related to the velocity of weathering  
305 front migration. Such inversion/disturbance of weathering polarity was not observed in  
306 previous analyses of the corresponding bulk soil samples (Gontier et al., 2015), most likely  
307 due to the analysis of the mere fine earth fraction (< 2 mm) and to the greater mass of the  
308 sample used for bulk analyses, which is expected to reduce small-scale heterogeneity. More  
309 unexpected, the U-series disequilibria are neither consistent with the weathering state of  
310 the grains based on the K/Fe ratio or on the remaining amount of biotite (Fig. 5). As for the  
311 relationship with depth, biotite extracted from the saprolite and the coarse shallow sample  
312 (20-30 cm > 200  $\mu\text{m}$ ) do not follow the observed trend.

313 Nevertheless, all U-series activity ratios demonstrate regular and self-consistent evolution  
314 when localization or weathering state based on major elements are not considered (Fig. 6).  
315 The observed decline in the ( $^{234}\text{U}/^{238}\text{U}$ ) ratio closely follows the increase in the ( $^{230}\text{Th}/^{234}\text{U}$ )  
316 ratio and the decrease in the ( $^{226}\text{Ra}/^{230}\text{Th}$ ) or the ( $^{226}\text{Ra}/^{238}\text{U}$ ) ratios. Likewise, the decrease in  
317 the ( $^{234}\text{U}/^{238}\text{U}$ ) ratio is anti-correlated with the increase in the ( $^{238}\text{U}/^{232}\text{Th}$ ) ratio (Fig. 7a). The  
318 isochron ( $^{230}\text{Th}/^{232}\text{Th}$ ) vs ( $^{238}\text{U}/^{232}\text{Th}$ ) diagram also shows a regular evolution of the samples  
319 compositions, albeit below the equiline (Fig. 7b). The nuclides mobility implied by these  
320 variations is discussed below (section 4.1).

321

### 322 **3.2 Selective treatments of the saprolite biotite**

323 The major element contents in the residual mineral after interlayer extraction are reported  
324 in Table 2. The significant decrease in K<sub>2</sub>O concentration (7 to 4 wt%) and the concurrent  
325 increase in Na<sub>2</sub>O concentration(0.7 to 6.2 wt%) suggest the exchange of K by Na and confirm  
326 the efficient extraction of the interlayer. U and Th percentages extracted during the 3  
327 successive extractions are reported in Table 4. The total amount of U and Th extracted is  
328 limited (~1 and 0.2 % of the total U and Th) and a rapid decrease in the proportions of U and  
329 Th extracted is observed over the 3 successive extractions, ranging from 0.7 to 0.05 % for U  
330 and from 0.15 to 0 % for Th.

331 The amount of U and Th adsorbed and/or associated with amorphous Fe-Mn-Al oxy-  
332 hydroxides was also found to be low: 2 % of the total U and 4 % of Th (Table 4). Despite the  
333 previously reported ligand-promoted dissolution of biotite by oxalate solutions (e.g., Haward  
334 et al., 2011), the low level of Mg release (0.4 %) precludes significant biotite dissolution  
335 during such extraction.

336

## 337 **4. Discussion**

### 338 **4.1 Origin of U/Th variability**

339 Patterns of U and Th content variability observed from the samples described above (Fig. 3  
340 and 4) cannot be explained by usual weathering processes during which U is usually highly  
341 mobile while Th is known to be very insoluble (Chabaux et al., 2008; Vigier and Bourdon,  
342 2011). A decrease of U/Th ratio is therefore expected during weathering process, in contrast  
343 with the evolution of the U/Th ratios observed in the analyzed samples (Fig. 4a). Issues  
344 concerning initial heterogeneity and/or the removal of typically immobile elements (e.g., Th  
345 and Ti) to explain the observed trends therefore arise in order to further model the observed  
346 U-series disequilibria. Heterogeneous initial U/Th ratios can indeed produce a trend similar  
347 to that observed along the equiline in the (<sup>230</sup>Th/<sup>232</sup>Th) vs (<sup>238</sup>U/<sup>232</sup>Th) isochron diagram (Fig.  
348 7b). However, in this diagram, whatever the initial positioning of the sample, the observed  
349 shift from the equiline involves an increase in the U/Th ratio and/or a decrease in the  
350 (<sup>230</sup>Th/<sup>232</sup>Th) isotopic ratio. An increase in the U/Th ratio due to a gain of U in these samples  
351 is highly unlikely in view of several of the following features: i) U content does not

352 significantly increase in samples with low amount of remaining biotite (or low K content)  
353 (Fig. 3); ii) the concurrent decrease in Ti and increase in U/Th (Fig. 4b) would imply a  
354 correlated loss of Ti with gain of U; iii) the 20-30 cm (50-200  $\mu\text{m}$ ) sample presents the  
355 highest U/Th ratio but the lowest ( $^{234}\text{U}/^{238}\text{U}$ ) activity ratio (= 0.73). A gain of  $^{238}\text{U}$  in this  
356 sample would therefore imply a lack of  $^{234}\text{U}$  gain (e.g., 30 % of gained  $^{238}\text{U}$  in this sample  
357 would require a ( $^{234}\text{U}/^{238}\text{U}$ ) input ratio of as low as 0.3); iv) the extraction of exchangeable  
358 cations using NaCl and of amorphous and poorly crystallized Fe-Mn-Al oxy-hydroxides using  
359 oxalate ammonium solution from the saprolite biotite with a high U/Th ratio, i.e.: sample  
360 that could be suspected to have gained some U, yielded a recovery value of less than 1 % of  
361 U for the exchangeable fraction and no more than 2 % of U for the amorphous oxy-  
362 hydroxides fraction, precluding the presence of significant amount of adsorbed U. A loss of  
363 Th (either  $^{230}\text{Th}$  relative to  $^{232}\text{Th}$  or  $^{232}\text{Th}$  relative to  $^{238}\text{U}$  or both) is therefore mandatory to  
364 explaining the positioning of the samples below the equiline in the ( $^{230}\text{Th}/^{232}\text{Th}$ ) vs  
365 ( $^{238}\text{U}/^{232}\text{Th}$ ) diagram. The ongoing decline in Th content observed in the most weathered  
366 samples (Fig. 3) denotes  $^{232}\text{Th}$  loss, but Th leaching was also independently assessed for  $^{230}\text{Th}$   
367 relative to  $^{238}\text{U}$  (section 4.3). Such loss implies a concurrent loss and/or heterogeneity of Ti  
368 to explain the U/Th vs Ti relationship (Fig. 4b). As suggested by the variability of U and Th  
369 contents in replicates of the saprolite biotite sample, some heterogeneity of the trace  
370 element contents in the study samples can be suspected, and the presence of Ti-oxides in  
371 some of our samples (Fig. 2) strongly supports this doubt. Accordingly the Ti contents of the  
372 study grains are inconsistent with major elements ( $\text{SiO}_2/\text{Al}_2\text{O}_3$  or  $\text{K}_2\text{O}/\text{Fe}_2\text{O}_3$  ratios for  
373 instance) and mineralogy. In addition, if a Ti initial homogeneous content and its immobility  
374 was assumed, the decrease of  $\text{TiO}_2$  content from 2.4 % (in the saprolite biotite) to 1.3 % in  
375 the fine 20-30cm (50- 200 $\mu\text{m}$ ) sample would imply the precipitation of about the same mass  
376 of secondary, Ti-depleted material than primary material (i.e. the mass must be multiplied  
377 by 2). This appears highly unlikely within a grain where the volume and fabric of the primary  
378 biotite mineral remain preserved. In contrast, the release of Ti from the crystallographic  
379 structure of biotites, through chemical weathering was previously reported (Cornu et al.,  
380 1999; Taboada et al., 2006). Hence, the use of Ti as reliable weathering proxy is not relevant  
381 in these samples.

382 Based on all these features, and despite the potential presence of slight initial  
383 heterogeneities, the observed U and Th contents variability seems therefore most likely

384 attributable to a preferential loss of Th relative to U Several previous studies have identified  
385 Th mobility in soil, usually linked to organic matter complexation (Dosseto et al., 2008;  
386 Rezzoug et al., 2009; Rihs et al., 2011; Keech et al., 2013; Gontier et al., 2015, Dosseto et al.,  
387 2019). In the present study, however, a similar Th mobility is observed from samples  
388 positioned at the bottom of the soil profile as well as at the surface. Such Th mobilization  
389 observed across the entire soil profile was already highlighted from corresponding bulk  
390 samples (Gontier et al., 2015) despite a significant decline in C organic content in seepage  
391 soil solutions with depth (Jaffrain, 2006; Cornelis et al., 2010) as well as in soil layers  
392 (Marechal et al., 2013; Rihs, Gontier et al., 2016). Alternatively, the relationship between  
393 U/Th and Ti (Fig. 4b) could suggest a removal of solid Ti- and Th- rich nanoparticles from  
394 accessory minerals. However, such an assumption cannot explain the preferential removal of  
395  $^{230}\text{Th}$  relative to  $^{238}\text{U}$  (section 4.3) as both nuclides are expected to be located within the  
396 same mineral fraction. These results echo various recent works that report Th mobility  
397 across different contexts where organic complexation appears to be precluded. For instance,  
398 Bosia et al. (2018) showed that zircons from Gandak River sediments (Himalaya) have  
399 undergone a loss of both  $^{230}\text{Th}$  and  $^{232}\text{Th}$  isotopes. Additional in-situ SIMS analyses of the  
400 Gandak River samples demonstrate that the Th depletion is not restricted to the grain  
401 surface, but instead continues 15-20  $\mu\text{m}$  below the mineral surface while the ( $^{234}\text{U}/^{238}\text{U}$ )  
402 ratios remain equal to 1 (Bosia, 2016). Menozzi (2016) and Dosseto et al. (2019) also  
403 reported a significant leaching of  $^{230}\text{Th}$  from quartz sampled in both granitic and sandstone  
404 saprolites at a depth of 2.5 m and in apparently pristine bedrocks (New South Wales,  
405 Australia). In contrast, a gain of  $^{232}\text{Th}$  (as well as U) was observed by these authors in the  
406 biotite separated grains from the granitic profile, highlighting, if needed, the influence of  
407 external-to-the-mineral factors on nuclides behavior in weathering profiles. Rihs et al. (2011)  
408 showed that the leaching constants of both Th isotopes in deep soil layers of the  
409 Strenghbach catchment (Vosges, France) are at least two orders lower than those observed  
410 in the shallowest soil layers where organic complexation has been identified. Clearly, these  
411 results suggest that the mechanism(s) of Th mobilization observed in weathering  
412 environments remain(s) poorly understood and need(s) further investigations.

413

#### 414 **4.2 Weathering signal recorded by U-series versus major elements.**

415 During water-rock interaction, U-series nuclides fractionation usually produces radioactive  
416 disequilibria in the U-series decay chain (Chabaux et al., 2008). Yet, major elements and U-  
417 series disequilibria data are opposing in the saprolite biotite and coarse 20-30 cm (> 200 μm)  
418 samples. These samples are indeed significantly out of radioactive equilibrium while major  
419 elements contents and mineralogical analyses suggest only minor patterns of weathering  
420 evolution (Fig. 5). For instance, saprolite biotite grains comprise 92 % of remaining biotite  
421 and 8 % of quartz (or 100 % of biotite with quartz excepted), without traces of secondary  
422 minerals (Fig. 2) and the coarse 20-30 cm (> 200 μm) grains contain the second highest  
423 amount of remaining biotite (75 %, quartz excepted). Yet, the low ( $^{234}\text{U}/^{238}\text{U}$ ), ( $^{230}\text{Th}/^{238}\text{U}$ )  
424 and ( $^{226}\text{Ra}/^{230}\text{Th}$ ) ratios observed in these samples (Table 3) imply a considerable removal of  
425  $^{234}\text{U}$ , but also of  $^{230}\text{Th}$  and  $^{226}\text{Ra}$ , thus involving significant water-mineral interactions not  
426 detected by major elements. Two mechanisms of non-stoichiometric nuclide removal could  
427 be assumed from the biotite: i) a direct ejection of daughter nuclides by alpha-recoil or ii) a  
428 leaching from the mineral interlayer. Owing to the large size of the separated grains (> 200  
429 μm), no models recently developed to estimate the alpha-recoil loss fraction (Depaolo et al.,  
430 2006, Maher et al., 2006b; Bourdon et al., 2009) predict a rate of ejection higher than 0.01,  
431 thus failing to explain a ( $^{234}\text{U}/^{238}\text{U}$ ) ratio as low as 0.76 – 0.79. In addition, Depaolo et al.  
432 (2006) compare the timescales of  $^{234}\text{U}$  alpha-recoil and mineral dissolution processes as  
433 follow:

434

$$435 \quad \frac{\tau_{\text{recoil}}}{\tau_{\text{dissolution}}} = \frac{R \times M}{^{234}\lambda \times L \times \rho} \quad [1]$$

436

437 where  $\tau_{\text{recoil}}$  and  $\tau_{\text{dissolution}}$  denote the timescales of alpha-recoil and mineral dissolution  
438 processes, respectively, R denotes the dissolution rate of the mineral (in  $\text{mol.m}^{-2}.\text{s}^{-1}$ ), M  
439 denotes the molar mass of biotite ( $\text{g.mol}^{-1}$ ),  $\lambda_{234}$  denotes the decay constant of  $^{234}\text{U}$  ( $\text{s}^{-1}$ ), L  
440 denotes the alpha-recoil distance of  $^{234}\text{Th}$  (m) and  $\rho$  denotes the mineral density ( $\text{g/m}^3$ ).

441 Using  $L = 30 \text{ nm}$  (Maher 2006b),  $\rho = 2.97 \text{ g.cm}^{-3}$  (Turpault and Trotignon, 1994),  $M = 445$   
442  $\text{g.mol}^{-1}$  and R the range of biotite field weathering rates reported by White and Brantley  
443 (2003) as  $1.3.10^{-16} - 7.9.10^{-15} \text{ mol.m}^{-2}.\text{s}^{-1}$ , this dimensionless number ranges from 7 to 445,

444 indicating that the timescale for  $^{234}\text{U}$  recoil is one or two orders of magnitude longer than  
445 that of the mineral's dissolution. This indicates that the mineral would dissolve before the  
446 alpha-recoil process could significantly deplete the  $^{234}\text{U}$  isotope from this mineral and  
447 therefore precludes significant  $^{234}\text{U}$  recoil from these minerals.

448 Alternatively, leaching from the mineral interlayer (hypothesis ii above) might be assumed.  
449 In view of the phyllosilicate structure of biotite, a significant implementation of  $^{234}\text{U}$  in the  
450 mineral interlayer space by alpha-recoil can be expected. Approximately 1.2 Ma after the  
451 mineral's formation, all  $^{234}\text{U}$  present in the mineral ensues from  $^{238}\text{U}$  decay and would  
452 therefore be located in the mineral following an alpha-recoil implementation. Based on a 2:1  
453 sheet and an interlayer thickness of 0.66 nm and 0.34 nm respectively (Dahl, 1996), simple  
454 geometric consideration predicts that roughly 30 % of the  $^{234}\text{U}$  produced through  $^{238}\text{U}$  decay  
455 would be located within the interlayer. Assuming such amount, the ( $^{234}\text{U}/^{238}\text{U}$ ) ratio  
456 measured from the saprolite biotite (= 0.76) would imply that the quasi-totality of interlayer  
457  $^{234}\text{U}$  was leached out. The interlayer extraction of this sample indeed confirms a low amount  
458 of interlayer U (< 1 % of U) that could be consistent with a previous depletion. However,  
459 initial  $\text{K}_2\text{O}$  content (7.8 %) within this sample was only slightly lower than in the  
460 unweathered mineral (9.4 %) determined by Mareschal (2008). In contrast, during interlayer  
461 extraction, a large amount of K was, as expected, removed ( $\text{K}_2\text{O}$  content dropped to 4 %  
462 after NaCl treatment). A previous leaching of  $^{234}\text{U}$  from the interlayer would therefore imply  
463 a nearly full removal of  $^{234}\text{U}$  without K release. Such disconnected fluxes could appear  
464 dubious. However, Wan et al. (2017) suggest that preferential dissolution from weaker  
465 surface defects on basal biotite surfaces produces a path for  $\text{CO}_2$  entry to the mineral  
466 interlayer more likely than simple diffusion from the edges. Such a process allows for  
467 mobility of elements from and out of the interlayers without concurrent K mobility. In  
468 addition, the U-series weathered-signature of the saprolite and the coarse 20-30 cm > 200  
469  $\mu\text{m}$  samples are actually consistent with their high  $\delta^{11}\text{B}$  isotopic composition (-26.8 and -23.5  
470 ‰ respectively while the value measured from the unweathered biotite is -31 ‰) reported  
471 by Voinot (2012). This author suggests that B isotopic composition evolves faster than  
472 mineral transformation and emphasizes nanoscale mechanisms that control B release. U-  
473 series, as B isotopes, therefore seem able to trace early weathering reactions before major  
474 elements and/or mineralogical proxies. The difference observed here between major and  
475 trace element signatures raises issues concerning the stoichiometric release of trace

476 elements during weathering. Trace elements are widely used to refine conditions of water-  
 477 rock interactions, e.g., Sr (Bullen et al., 1997, White 2017), B (Lemarchand et al., 2012), Li  
 478 (Millot et al., (2010)), and U (Maher et al. 2004, 2006a,b), and the assumption of the  
 479 stoichiometric release of these elements during mineral weathering constitutes a key point.  
 480 Several studies have addressed this issue but have generated contradictory results for non-  
 481 radiogenic as well as radiogenic isotopes. For instance, the stoichiometric or non-  
 482 stoichiometric release of non-radiogenic <sup>86</sup>Sr seems to depend on the mineral considered: K-  
 483 feldspar (Bullen et al., 1997; Brantley et al., 1998) labradorite or biotite (Taylor et al., 2000a,  
 484 b). Similarly, Olander and Eyal (1990) demonstrate a non-stoichiometric release of <sup>238</sup>U and  
 485 <sup>232</sup>Th from monazite over a 6.8-year experiment while Andersen et al. (2009) suggest a  
 486 congruent dissolution of granite minerals with respect to <sup>238</sup>U. For radiogenic isotopes,  
 487 Bullen et al. (1997) report a non-stoichiometric release of <sup>87</sup>Sr while Andersen et al. (2009)  
 488 highlight transient features of the non-stoichiometric release of <sup>234</sup>U. This transient issue,  
 489 also identified by Brantley et al. (1998) for Sr isotopes, is fundamental, as most of the  
 490 reported results arise from experimental studies, i.e., short-term relative to a natural  
 491 weathering timescale. In contrast, the results of the present study emphasize the early and  
 492 preferential release of U-series nuclides relative to the major element over a natural  
 493 weathering timescale.

494

### 495 **4.3. Long-term weathering rate of the biotite**

496 To estimate the duration of mineral weathering, an open model was used (Vigier et al.,  
 497 2001) where decay and leaching are considered as follows:

498

$$\begin{aligned}
 499 \quad \frac{d^{238}U}{dt} &= -(\lambda_{238U} + k_{238U})^{238}U \\
 500 \quad & \left. \vphantom{\frac{d^{238}U}{dt}} \right\} [2] \\
 501 \quad \frac{d^nN}{dt} &= -(\lambda_n + k_n)^nN + \lambda_{n-1}^{n-1}N \\
 502 \quad & \left. \vphantom{\frac{d^nN}{dt}} \right\}
 \end{aligned}$$

503 where <sup>n</sup>N stands for the number of <sup>234</sup>U, <sup>230</sup>Th or <sup>226</sup>Ra atoms, and <sup>n-1</sup>N the abundance of the  
 504 corresponding parent nuclide.  $k_n$  and  $\lambda_n$  ( $y^{-1}$ ) are the leaching and decay constants of the  
 505 nuclide <sup>n</sup>N, respectively.

506

507 No gain of nuclides was used in this model as justified for U in the above section (4.1). For  
508  $^{230}\text{Th}$  and  $^{226}\text{Ra}$ , the high content of these nuclides in the samples (resulting from high U  
509 content i.e., 40-50 ppm) renders them much less sensitive to potential gains. Such a model is  
510 consistent with the commonly observed mechanism of biotite alteration to kaolinite or  
511 vermiculite through epitaxial weathering without external gain (White, 2002). The 120-140  
512 cm sample, characterized by the closest-equilibrium state, was used as initial material.  
513 Owing to uncertainties related to the coarse 20-30 cm ( $> 200 \mu\text{m}$ ) and saprolite samples  
514 described above, the two samples were discarded for the fit and data from the 120-140 cm,  
515 120-130 cm, 110-120 cm and the fine 20-30 cm ( $< 200 \mu\text{m}$ ) samples only were fitted by the  
516 model. We solved the set of model equations (2) using the differential equation solver  
517 (ode45) available through Matlab<sup>®</sup> commercial software. We randomly selected 500 sets of  
518 initial  $k_n$  values in the range  $10^{-6}$  to  $10^{-3} \text{y}^{-1}$  and solved the differential equations over 500 ky.  
519 Each initial set of leaching constants was adjusted using the Matlab<sup>®</sup> lsqnonlin function to fit  
520 the measured ( $^{234}\text{U}/^{238}\text{U}$ ), ( $^{230}\text{Th}/^{234}\text{U}$ ) and ( $^{226}\text{Ra}/^{238}\text{U}$ ) ratios of each sample. In view of  
521 uncertainties related to the homogenous initial U content discussed above, the evolution of  
522 U concentrations in the samples was not used as a model parameter. Finally, only the sets of  
523 parameters matching the measured ratios within  $\pm 2\text{SD}$  uncertainty levels and yielding  
524  $k_{234}/k_{238}$  ratios lower than 5 were retained. The range of solutions describing the measured  
525 data is reported in Table 5. Radium presents the highest leaching constant ( $k^{226}\text{Ra} \approx 10^{-4} \text{y}^{-1}$ )  
526 within a very narrow range consistent with the short half-life of this nuclide. As one striking  
527 feature of these solutions, leaching constants of  $^{230}\text{Th}$  are lower than those of  $^{234}\text{U}$  but are  
528 higher than those of  $^{238}\text{U}$  ( $k^{238}\text{U}/k^{230}\text{Th} < 1$ , Fig. 8). These results obtained without any  
529 constraints on  $^{230}\text{Th}$  mobility are fully consistent with the preferential leaching of  $^{232}\text{Th}$   
530 relative to  $^{238}\text{U}$ , highlighted above.

531 The amount of time required to evolve from the initial sample (120-140 cm) to the most out-  
532 of-equilibrium sample positioned in the shallowest soil layer (20-30 cm,  $< 200 \mu\text{m}$ ) ranges  
533 from 6 to 52 ky. The two extreme models, i.e., leading to a duration of 6 and 52 ky  
534 respectively, are represented in Fig. 6, along with the measured data. While excluded from  
535 best-fit optimization, the 20-30 cm ( $> 200 \mu\text{m}$ ) and saprolite biotites are also reported in the  
536 figure, and were found to be consistent with the retained models.

537 For the two reported models, the evolution of the ( $^{238}\text{U}/^{232}\text{Th}$ ) and ( $^{230}\text{Th}/^{232}\text{Th}$ ) ratios can be  
 538 reproduced assuming a leaching of  $^{232}\text{Th}$  (Eq. 2 applied to  $^{232}\text{Th}$ ). Leaching constants of  $^{232}\text{Th}$   
 539 yielding the best-fit to the data are reported in Table 5, and corresponding models are  
 540 reported in Fig 7a and 7b. The required  $k^{232}\text{Th}$  leaching constants are higher than those of  
 541  $k^{238}\text{U}$  and  $k^{230}\text{Th}$ . The evolution of the ( $^{230}\text{Th}/^{232}\text{Th}$ ) vs ( $^{238}\text{U}/^{232}\text{Th}$ ) ratios observed across all  
 542 of the samples can be satisfactorily described with both models (Fig. 7b). In contrast, the  
 543 models failed to reproduce the ( $^{234}\text{U}/^{238}\text{U}$ ) vs ( $^{238}\text{U}/^{232}\text{Th}$ ) ratios of the 20-30 cm (> 200  $\mu\text{m}$ )  
 544 and saprolite samples and are even questionable for the 110-120 cm sample (Fig. 7a).  
 545 However, a slight change in the initial ( $^{238}\text{U}/^{232}\text{Th}$ ) ratio (e.g., 0.37 instead of 0.48) allows for  
 546 the reproduction of the ( $^{234}\text{U}/^{238}\text{U}$ ) vs ( $^{238}\text{U}/^{232}\text{Th}$ ) ratios of the saprolite and 110-120 cm  
 547 samples while a minor change in the ( $^{230}\text{Th}/^{232}\text{Th}$ ) vs ( $^{238}\text{U}/^{232}\text{Th}$ ) pattern was induced by this  
 548 lower initial ( $^{238}\text{U}/^{232}\text{Th}$ ) ratio (Fig. 7b). These results reinforce the hypothesis of potential  
 549 initial U/Th heterogeneity in the biotite samples presented above, but demonstrate the low  
 550 sensitivity of the so-called ( $^{230}\text{Th}/^{232}\text{Th}$ ) vs ( $^{238}\text{U}/^{232}\text{Th}$ ) isochron diagram to such  
 551 heterogeneity. Figure 7b shows that the variation of the ( $^{230}\text{Th}/^{232}\text{Th}$ ) is, to first order, driven  
 552 by time rather than initial U/Th ratio. Yet, the models reported in Fig. 6, the corresponding  
 553 elapsed time, and therefore the deduced weathering rates calculated below are completely  
 554 independent of this heterogeneity.

555

556 The biotite weathering rate was calculated from the minimum and maximum amount of  
 557 time required for evolution from 110-120 cm to 20-30 cm (< 200  $\mu\text{m}$ ) samples (5.8 and 49 ky  
 558 using models 1 and 2, respectively). The 120-140 cm sample, used as initial material in the U-  
 559 series models, could not be used for weathering rate determination, as the fraction of the  
 560 remaining biotite mineral was not resolved in this sample. However, the 110-120 cm  
 561 sample presents a very similar U-series signature (Fig. 6). The amount of dissolved mineral  
 562 was calculated through the estimation of the biotite mass fraction remaining in the grains  
 563 (Voinot, 2012), i.e., 60 % and 28 % in the 110-120 cm and 20-30 cm (< 200  $\mu\text{m}$ ) samples,  
 564 respectively, (Table 3) assuming an isovolumetric weathering. The weathering rate, R, was  
 565 then calculated as follows:

566

$$567 \quad R = \frac{m_i - m_f}{\frac{M}{T \times S}} \quad [3]$$

568

569 where  $m_i$  and  $m_f$  are the initial and final mass of the biotite per g of sample respectively,  $M$  is  
570 the molar mass of biotite, calculated from structural formulae of the studied biotite  
571 established by Marechal (2008) ( $455 \text{ g.mol}^{-1}$ ),  $T$  is the weathering duration determined by U-  
572 series models and  $S$  is the measured specific surface area ( $6 \text{ m}^2.\text{g}^{-1}$ ).

573 This calculation yields a weathering rate  $R$  ranging from  $6.5 \times 10^{-16} \text{ mol.m}^{-2}.\text{s}^{-1}$  (model 1) to  
574  $7.8 \times 10^{-17} \text{ mol.m}^{-2}.\text{s}^{-1}$  (model 2). The isovolumetric weathering assumption may lead to an  
575 overestimation of the dissolved mass and thus to an underestimation of weathering rates.  
576 However, such isovolumetric weathering is a common feature observed in saprolites  
577 developed in tropical and temperate environments (White et al., 1998, 2002), and the  
578 calculated rates are fully consistent with field weathering rates of biotite previously reported  
579 from a variety of lithology and climatic regimes (Fig. 9). It should be noted that the highest  
580 rates reported in Fig. 9 for timespans of  $10^4$  and  $3 \times 10^5$  y correspond to the tropical Rio  
581 Icacos Watershed (Puerto Rico) (White et al., 2002, Murphy et al., 1998; Buss et al., 2008).  
582 The rate calculated from model 1 in the present study was found to be similar to the rate  
583 derived from sedimentary chronosequences of the Rhône and Oberaar Glaciers (Swiss Alp)  
584 reported by Föllmi et al. (2009) ( $\approx 2 \times 10^{-15} \text{ mol.m}^{-2}.\text{s}^{-1}$  over a 10 ky timespan, corresponding  
585 to rates based on the total mineral surface area rather than the edge surface to compare to  
586 the present and previously reported studies). These results demonstrate that U-series can  
587 provide a useful tool for long-term mineral rate determination, as suggested by Dosseto et  
588 al. (2014, 2019). Actually, the assessment of a long-term field mineral dissolution rate is  
589 difficult and is classically based on dissolved fluxes exported by rivers and/or aquifers or on  
590 changes in the regolith composition coupled with cosmonuclide-based denudation rate  
591 estimation (review given in White and Buss, 2014). Considerable uncertainties affect these  
592 approaches, hampering the resolution of long-standing assessments of the apparent  
593 discrepancy between laboratory and field weathering rates (Paces, 1983; Taylor and Blum,  
594 1995; White and Brantley, 2003; Maher et al., 2004, 2009; Hellman et al., 2012; White et al.,  
595 2017). U-series disequilibria of regolith-separated minerals offer a new direct approach that  
596 could be applied to other common silicate minerals.

597

598 **4.4. Comparison to short-term weathering rates**

599 We previously studied nearby soil profiles from the same experimental site, where the  
600 native forest was partially clear-felled in 1976 and replaced with monospecific Oak and  
601 Douglas Fir stands (Rihs, Gontier et al., 2016). U- and Th-series disequilibria were measured  
602 from bulk soils developed under the native forest (as in the present study) and from the two  
603 replanted stands. We found that tree substitution (the change in specie as well as associated  
604 temporary soil denudation) had yielded a considerable dissolution of biotites in the soil  
605 under the replanted Oaks. The mean biotite weathering rate deduced from this recent  
606 substitution was found to be equal to  $1.1 \times 10^{-12} \text{ mol.g}^{-1}.\text{s}^{-1}$ , corresponding to a value of  
607  $1.8 \times 10^{-13} \text{ mol.m}^{-2}.\text{s}^{-1}$  with a specific surface area  $S = 6 \text{ m}^2.\text{g}^{-1}$ . This rate is roughly 2 or 3 orders  
608 of magnitude higher than the long term rate calculated above from the same site without  
609 vegetation substitution but is consistent with the rate that could be extrapolated for a 35-  
610 year weathering period from the time-dependent relationship proposed by White and  
611 Brantley (2003) or from rates deduced from sedimentary chronosequences of the Rhône and  
612 Oberaar Glaciers at 140 and 270 y (Föllmi et al., 2009) (Fig. 9). This result is noteworthy as it  
613 probes a period of time, i.e., 35 years that is too long for laboratory experiments and too  
614 short for classical field, long-term studies, leading to a critical lack of data. This shows that  
615 short-term laboratory experiments can be representative of field processes, and suggests  
616 that mineral weathering reactivation, similar to what is observed in laboratory experiments,  
617 may naturally occur in soils, in response to perturbation, i.e., land cover change in the  
618 present case.

619

## 620 **5. Conclusion**

621 Long-term field weathering rate of biotite was determined using U-series disequilibria  
622 measured from several grains extracted from a granitic soil profile at different depths. The  
623 grains correspond to the pseudomorphosis of parent biotites, including weathering products  
624 retained within the unchanged volume and fabric of the parent minerals. The remaining  
625 parent biotite ranges from 100 % to 28 % in the study samples.

626 Despite potential initial U/Th content heterogeneities in the samples, the U-series activity  
627 ratios describe a regular and self-consistent pattern of weathering evolution. This  
628 weathering evolution however involves a significant loss of Th, highlighting that the  
629 mechanism of Th mobilization observed in weathering environments remains poorly  
630 understood and deserves further investigations. In addition, some samples show significant

631 U-series disequilibria while major element contents and mineralogical analyses show only  
632 minor signs of weathering. This discrepancy between the "U-series-derived- weathered -  
633 stage" and macroscopic features emphasizes a nanoscale mechanism that controls U-series  
634 nuclides release and suggests that these nuclides can trace early weathering reactions  
635 before major elements and/or mineralogical proxies.

636 An open-system model based on radioactive decay and leaching rates was applied to  
637 successfully describe ( $^{234}\text{U}/^{238}\text{U}$ ), ( $^{234}\text{U}/^{230}\text{Th}$ ), and ( $^{226}\text{Ra}/^{230}\text{Th}$ ) disequilibria evolution and to  
638 infer the amount of time required for the less weathered sample, located in deep soil layers  
639 to evolve into the most out-of-equilibrium sample found in the shallowest soil layer. The  
640 model demonstrates the low sensitivity of the ( $^{230}\text{Th}/^{232}\text{Th}$ ) vs ( $^{238}\text{U}/^{232}\text{Th}$ ) diagram to U/Th  
641 initial heterogeneity in the samples. The biotite weathering rate was deduced from the  
642 determined duration and the amount of mineral dissolved. This latter was calculated  
643 through an estimation of the biotite parent mineral remaining in the analyzed grains (Voinot,  
644 2012). The deduced weathering rate ranges from  $7.8 \times 10^{-17} \text{ mol.m}^{-2}.\text{s}^{-1}$  to  $6.5 \times 10^{-16} \text{ mol.m}^{-2}.\text{s}^{-1}$ ,  
645 <sup>1</sup>, which is perfectly consistent with long-term field weathering rates of biotite previously  
646 reported. These results demonstrate that U-series disequilibria of regolith-separated  
647 minerals offer a useful and direct means of determining long-term weathering rates. In  
648 addition, we previously showed that experimental vegetation substitution occurring 35 years  
649 ago close to the study soil profile spurred a considerable dissolution of biotites under Oak  
650 replaced stands (Rihs, Gontier et al., 2016). The substitution-induced weathering rate of the  
651 biotite measured under the replaced vegetation was found to be 2 or 3 orders of magnitude  
652 higher than the long-term rate obtained through the present study but is consistent with the  
653 rate that can be extrapolated from the time-dependent relationship proposed by White and  
654 Brantley (2003). These results document a decrease in silicate weathering rates from long-  
655 (10,000s of years) and short-term (10s of years) weathering events for the same site. They  
656 show that short-term laboratory experiments can be representative of field processes and  
657 suggest that some processes of mineral weathering reactivation, similar to that observed  
658 during laboratory experiments, may naturally occur in soils, in response to short-term  
659 perturbation such as land cover change.

660

661 **Acknowledgements:** The authors acknowledge the SOERE FORET and ANAEE networks,  
662 Arnaud Legout and the INRA-BEF (Biogéochimie des Ecosystèmes Forestiers) team for

663 managing the Breuil- SORE site and sampling and mineral separation, and René Boutin  
664 (LHyGeS) for conducting ICP analyses. The constructive comments of two anonymous  
665 reviewers helped to improve the manuscript. This work was financially supported by the  
666 INSU- Syster Program. This research is an EOST contribution.

667

## 668 **References**

- 669 Ackerer J., Chabaux F., Van der Woerd J., Viville D., Pelt E., Kali E., Lerouge C., Ackerer P., di  
670 Chiara Roupert R., Négrel P. (2016) Regolith evolution on the millennial timescale from  
671 combined U–Th–Ra isotopes and in situ cosmogenic  $^{10}\text{Be}$  analysis in a weathering  
672 profile (Strengbach catchment, France). *Earth Planet. Sci. Lett.* 453, 33–43.
- 673 Andersen M.B., Erel Y., Bourdon B. (2009) Experimental evidence for  $^{234}\text{U}$ – $^{238}\text{U}$   
674 fractionation during granite weathering with implications for  $^{234}\text{U}/^{238}\text{U}$  in natural waters.  
675 *Geochim. Cosmochim. Acta* 73, 4124–4141.
- 676 Berner R.A. (1997) The rise of plants and their effect on weathering and atmospheric  $\text{CO}_2$ .  
677 *Science* 276, 544–546.
- 678 Bosia C. (2016) Les séries radioactives de l'uranium dans les sédiments de la rivière Gandak  
679 (Himalaya): de la roche totale aux analyses in situ sur les minéraux séparés. Ph. D. thesis,  
680 Strasbourg Univ.
- 681 Bosia C., Chabaux F., Pelt E., Cogez A., Stille P., Deloule E., France-Lanord C. (2018) U-series  
682 disequilibria in minerals from Gandak River sediments (Himalaya). *Chem. Geol.* 477, 22–  
683 34.
- 684 Bourdon B., Bureau S., Andersen M. B., Pili E. and Hubert A. (2009) Weathering rates from  
685 top to bottom in a carbonate environment. *Chem. Geol.* 258, 275–287.
- 686 Brantley S.L., Chesley J.T., Stillings L.L. (1998) Isotopic ratios and release rates of strontium  
687 measured from weathering feldspars. *Geochim. Cosmochim. Acta* 62, 1493–1500.
- 688 Bullen T., White A., Blum A., Harden J., Schulz M. (1997) Chemical weathering of a soil  
689 chronosequence on granitoid alluvium: II. Mineralogic and isotopic constraints on the  
690 behavior of strontium. *Geochim. Cosmochim. Acta* 61, 291–306.
- 691 Buss H.L., Chapela Lara M. Moore O.W., Kurtz A.C., Schulz M.S., White A.F. (2017)  
692 Lithological influences on contemporary and long-term regolith weathering at the  
693 Luquillo Critical Zone Observatory. *Geochim. Cosmochim. Acta* 196, 224–251.
- 694 Buss H.L., Sak P.B., Webb S.M., Brantley S.L. (2008) Weathering of the Rio Blanco quartz  
695 diorite, Luquillo Mountains, Puerto Rico: coupling oxidation, dissolution, and fracturing.  
696 *Geochim. Cosmochim. Acta* 72, 4488–4507.
- 697 Calvaruso, C., Mareschal, L., Turpault, M.-P., Leclerc, E., (2009). Rapid Clay Weathering in the  
698 Rhizosphere of Norway Spruce and Oak in an Acid Forest Ecosystem. *Soil Sci. Soc. Am. J.*  
699 73, 331–338.
- 700 Carpentier M., Gannoun A., Pin C., Sigmarsson O., (2016). New thorium isotope ratio  
701 measurements in silicate reference materials: A-THO, AGV-2, BCR-2, BE-N, BHVO-2 and  
702 BIR-1. *Geostand. Geoanal. Res.* 40, 239–256

703 Chabaux F., Ben Othman D., J.L. Birck (1994) A new Ra-Ba chromatographic separation and  
704 its application for the Ra mass spectrometric measurement in recent volcanic rocks.  
705 Chem. Geol. 114, 191-197. Erratum (1994) Chem. Geol. 116, 301.

706 Chabaux F., Blaes E., Stille P., di Chiara Roupert R., Pelt E., Dosseto A., Ma L., Buss H.L. and  
707 Brantley S.L. (2013) Regolith formation rate from U-series nuclides: Implications from  
708 the study of a spheroidal weathering profile in the Rio Icacos watershed (Puerto Rico).  
709 Geochim. Cosmochim. Acta 100, 73-95.

710 Chabaux F., Bourdon B. and Riotte J. (2008) U-Series Geochemistry in Weathering Profiles,  
711 River Waters and Lakes. In: *Radioactivity in the Environment* (Eds. S. Krishnaswami and  
712 J.K. Cochran). Elsevier, 49-104.

713 Chabaux F., Dequincey O., Lévêque J.-J., Leprun J.-C., Clauer N., Riotte J. and Paquet H.  
714 (2003b) Tracing and dating recent chemical transfers in weathering profiles by trace-  
715 element geochemistry and  $^{238}\text{U}$ - $^{234}\text{U}$ - $^{230}\text{Th}$  disequilibria: the example of the Kaya lateritic  
716 toposequence (Burkina-Faso). C. R. Geosci. 335, 1219-1231.

717 Chabaux F., Riotte J. and Dequincey O. (2003a) Fractionation during weathering and river  
718 transport. *Reviews in Mineralogy and Geochemistry* 52, 533-576.

719 Cheng, H., Edwards, R.L., Hoff, J., Gallup, C.D., Richards, D.A., Asmerom, Y. (2000). The half-  
720 lives of uranium-234 and thorium-230. Chem. Geol. 169, 17–33.

721 Clow D.W., Drever J.I. (1996) Weathering rates as a function of flow through an alpine soil.  
722 Chem. Geol. 132, 131 – 141.

723 Cogez A., Herman F., Pelt E., Reuschlé T., Morvan G., Darvill C.M., Norton K.P., Christl M.,  
724 Märki L., Chabaux F. (2018) U–Th and  $^{10}\text{Be}$  constraints on sediment recycling in  
725 proglacial settings, Lago Buenos Aires, Patagonia. Earth Surf. Dynam., 6, 121–  
726 140.

727 Condomines, M., Tanguy, J.C., Michaud, V., (1995). Magma dynamics at Mt Etna:  
728 Constraints from U–Th–Ra–Pb radioactive disequilibria and Sr isotopes in historical  
729 lavas. Earth and Planet. Sci. Lett. 132, 25–41.

729 Cornelis, J.T., Ranger, J., Iserentant, A., Delvaux, B., (2010). Tree species impact the  
730 terrestrial cycle of silicon through various uptakes. Biogeochemistry. 97, 231-245.

731 Cornu S., Lucas Y., Lebon E., Ambrosi J. P., Luizao F., Rouiller J., Bonnay M. and Neal C. (1999)  
732 Evidence of titanium mobility in soil profiles, Manaus, central Amazonia. Geoderma 91,  
733 281–295.

734 Dahl P.S. (1996) The crystal-chemical basis for Ar retention in micas: inferences  
735 from interlayer partitioning and implications for geochronology. Contrib Mineral Petrol  
736 123, 22–39.

736 Delanghe, D., Bard, E., Hamelin, B. (2002). New TIMS constraints on the uranium-238 and  
737 uranium-234 in seawaters from the main ocean basins and the Mediterranean Sea.  
738 Marine Chem. 80, 79–93.

739 DePaolo D.J., Maher K., Christensen J.N. and McManus J. (2006) Sediment transport time  
740 measured with U-series isotopes: Results from ODP North Atlantic drift site 984. Earth  
741 Planet. Sci. Lett. 248, 394-410.

742 Dequincey, O., Chabaux, F., Clauer, N., Sigmarsson, O., Liewig, N., Leprun, J.C., (2002).  
743 Chemical mobilizations in laterites: evidence from trace elements and  $^{238}\text{U}$ - $^{234}\text{U}$ - $^{230}\text{Th}$   
744 disequilibria. *Geochim. Cosmochim. Acta.* 66, 1197-1210.

745 Dosseto A., Buss H. L. and Chabaux F. (2014) Age and weathering rate of sediments in small  
746 catchments: the role of hillslope erosion. *Geochim. Cosmochim. Acta* 132, 238–258.

747 Dosseto A., Turner S.P., Chappell J. (2008) The evolution of weathering profiles through time:  
748 New insights from uranium-series isotopes. *Earth Planet. Sci. Lett.* 274, 359-371.

749 Dosseto, A, Menozzi D., Kinsley L.P.J. (2019) Age and rate of weathering determined using  
750 uranium-series isotopes: Testing various approaches. *Geochim. Cosmochim. Acta* 246,  
751 213-233.

752 Dosseto, A., Buss, H.L., Suresh, P.O. (2012) Rapid regolith formation over volcanic bedrock  
753 and implications for landscape evolution. *Earth Planet. Sci. Lett.* 337–338, 47-55.

754 Drever J.I. and Hurcomb D.R. (1986) Neutralization of atmospheric acidity by chemical  
755 weathering in an alpine drainage basin in the North Cascade Mountains. *Geology* 14,  
756 221-224.

757 Fichter, J., Bonnaud P., Turpault M.P. and Ranger J. (1998) Quantitative determination of  
758 minerals in acid forest soils of granite. *J. Plant Nutr. Soil Sci.* 161, 129-39.

759 Gaillardet, J., Dupré, B., Louvat, P., and Allègre, C. J. (1999) Global silicate weathering and  
760 CO<sub>2</sub> consumption rates deduced from the chemistry of large rivers. *Chemical Geology*  
761 159, 3-30.

762 Ghaleb, B., Pons-Branchu, E., Deschamps, P. (2004). Improved method for radium extraction  
763 from environmental samples and its analysis by thermal ionization mass spectrometry. *J.*  
764 *Anal. At. Spectrom.* 7, 906–910.

765 Gontier, A., Rihs, S., Chabaux, F., Lemarchand, D., Pelt, E., Turpault, M-P. (2015). Lack of  
766 bedrock grain size influence on the soil production rate. *Geochim. Cosmo. Acta.* 166,  
767 146-164.

768 Govindaraju, K. (1994). Compilation of working values and sample description for 383  
769 geostandards. *Geostandards Newsletter* 18, 1–158.

770 Granet, M., Chabaux, F., Stille, P., France-Lanord, C., Pelt, E. (2007). Time-scales of  
771 sedimentary transfer and weathering processes from U-series nuclides: Clues from the  
772 Himalayan rivers. *Earth Planet. Sci. Lett.* 261, 389-406.

773 Haward S.J., Smits M.M., Vala Ragnarsdottir K., Leake J.R., Banwart S.A. McMaster T.J.  
774 (2011), In situ atomic force microscopy measurements of biotite basal plane reactivity in  
775 the presence of oxalic acid. *Geochim. Cosmochim. Acta* 75, 6870–6881.

776 Hellmann, R., Wirth, R., Daval, D., Barnes, J.-P., Penisson, J.-M., Tisserand, D., Epicier, T.,  
777 Florin, B., Hervig, R.L. (2012) Unifying natural and laboratory chemical weathering with  
778 interfacial dissolution–reprecipitation: a study based on the nanometer-scale chemistry  
779 of fluid–silicate interfaces. *Chem. Geol.* 294–295, 203–216

780 Hinsinger P., Jaillard B. and Dufey J.E. (1992) Rapid Weathering of a Trioctahedral Mica by  
781 the Roots of Ryegrass. *Soil Sci. Soc. Am. J.* 56, 977-982.

782 Hochella Jr., M.F., Banfield, J.F., (1995). Chemical weathering of silicates in nature: a  
783 microscopic perspective with theoretical considerations. In: Ribbe, P.H. (Ed.), Chemical  
784 Weathering Rates of Silicate Minerals. Reviews in Mineralogy. Mineralogical Society of  
785 America, Washington, D.C., pp. 353–406.

786 Holden N.E. (1990) Total half-lives for selected nuclides. Pure Appl. Chem. 6, 941–958.

787 Jaffey A.H., Flynn K.F., Glendenin L.E., Bentley W.C., Essling A.M. (1971) Precision  
788 measurement of half-lives and specific activities of  $^{235}\text{U}$  and  $^{238}\text{U}$ . Phys. Rev. C 4, 1889–  
789 1906.

790 Jaffrain J. (2006) Effet des essences forestières sur le fonctionnement organo-minéral d'un  
791 sol acide: observations et modélisation. Ph. D. Thesis, Nancy I Univ.

792 Jeanbrun, M., Pourcelot, L., Mercat, C., Boulet, B., Pelt, E., Chabaux, F., Cagnat, X., Gauthier-  
793 Lafaye, F. (2012). Potential sources affecting the activity concentrations of  $^{238}\text{U}$ ,  $^{235}\text{U}$ ,  
794  $^{232}\text{Th}$  and some decay products in lettuce and wheat samples. J. Environ. Monit. 14,  
795 2902-2912.

796 Keech, A.R., West, A.J., Pett-Ridge, J.C., and Henderson, G.M., (2013) Evaluating U-series  
797 tools for weathering rate and duration on a soil sequence of known ages. Earth Planet.  
798 Sci. Lett. 374, 24-35.

799 Kigoshi K. (1971) Alpha recoil thorium-234: dissolution into water and uranium-  
800 234/uranium-238 disequilibrium in nature. Science 173, 47–49

801 Koornneef J.M., Stracke A., Aciego S., Reubi O., Bourdon B. (2010) A new method for U–Th–  
802 Pa–Ra separation and accurate measurement of  $^{234}\text{U}$ – $^{230}\text{Th}$ – $^{231}\text{Pa}$ – $^{226}\text{Ra}$  disequilibria in  
803 volcanic rocks by MC-ICPMS. Chem. Geol. 277, 30–41.

804 Lemarchand, D., Cividini, D., Turpault, M.P., Chabaux F. (2012) Boron isotopes in different  
805 grain size fractions: Exploring past and present water–rock interactions from two soil  
806 profiles (Strengbach, Vosges Mountains) Geochim. Cosmo. Acta 98, 78-93.

807 Leyval C. and Berthelin J. (1991) Weathering of a Mica by Roots and Rhizospheric  
808 Microorganisms of Pine. Soil Sci. Soc. Am. J. 55, 1009-1016.

809 Ma, L., Chabaux, F., Pelt, E., Blaes, E., Jin, L., Brantley, S. (2010) Regolith production rates  
810 calculated with uranium-series isotopes at Susquehanna/Shale Hills Critical Zone  
811 Observatory. Earth Planet. Sci. Lett. 297, 211-225.

812 Ma, L., Chabaux, F., Pelt, E., Granet, M., Sak, P.B., Gaillardet, J., Lebedeva, M., Brantley, S.L.,  
813 (2012). The effect of curvature on weathering rind formation: Evidence from Uranium-  
814 series isotopes in basaltic andesite weathering clasts in Guadeloupe. Geochim.  
815 Cosmochim. Acta 80, 92-107.

816 Ma, L., Chabaux, F., West, N., Kirby, E., Jin, L., Brantley, S. (2013) Regolith production and  
817 transport in the Susquehanna Shale Hills Critical Zone Observatory, Part 1: Insights from  
818 U-series isotopes. Journal of Geophysical Research, Earth Surface. 118, 722-740.

819 Maher K., DePaolo D.J., Christensen J.N. (2006b) U–Sr isotopic speedometer: Fluid flow and  
820 chemical weathering rates in aquifers. Geochim. Cosmochim. Acta 70, 4417–4435.

821 Maher K., DePaolo D.J., Lin C-F. (2004) Rates of silicate dissolution in deep-sea sediment: in  
822 situ measurement using  $^{234}\text{U}/^{238}\text{U}$  of pore fluids. *Geochim Cosmochim Acta* 68, 4629–  
823 4648.

824 Maher K., Steefel C., White A.F., Stonestrom D.A. (2009) The role of reaction affinity and  
825 secondary minerals in regulating chemical weathering rates at the Santa Cruz Soil  
826 Chronosequence, California. *Geochim. Cosmochim. Acta* 73, 2804–2831.

827 Maher K., Steefel C.I., DePaolo D.J., Viani B.E. (2006a) The mineral dissolution rate  
828 conundrum: insights from reactive transport modeling of U isotopes and pore fluid  
829 chemistry in marine sediments. *Geochim Cosmochim Acta* 70, 337–363.

830 Mareschal, L., (2008). Effet des substitutions d'essences forestières sur l'évolution des sols et  
831 de leur minéralogie: bilan après 28 ans dans le site expérimental de Breuil (Morvan). Ph.  
832 D Thesis, Nancy I Univ.

833 Mareschal, L., Bonnaud, P., Turpault, M.P., Ranger, J., (2010). Impact of common European  
834 tree species on the chemical and physicochemical properties of fine earth: an unusual  
835 pattern. *Eur. J. Soil Sci.* 61, 14-23.

836 Mareschal, L., Ranger, J., Turpault, M.-P. (2015). Effect of granite crystal grain size on soil  
837 properties and pedogenic processes. *Geoderma* 249-250, 12-20.

838 Martin D., Lal T., Sachdev C.B. and Sharma J.P. (2010) Soil organic carbon storage changes  
839 with climate change, landform and land use conditions in Garhwal hills of the Indian  
840 Himalayan mountains. *Agriculture, Ecosystems & Environment* 138, 64-73.

841 Menozzi D. (2016) Assessment of Sequential Extraction and Mineral Separation for studying  
842 Uranium-Series Isotopes in Regolith. Ph D thesis. Univ Wollongong, Australia.

843 Meunier A. (2005) *Clays*. Springer Berlin.

844 Millot R., Vigier N., Gaillardet J. (2010) Behaviour of lithium and its isotopes during  
845 weathering in the Mackenzie Basin, Canada. *Geochim. Cosmo. Acta* 74 3897-3912

846 Murphy S.F., Brantley S.L., Blum A.E., White A.F., Dong H. (1998) Chemical weathering in a  
847 tropical watershed, Luquillo Mountains, Puerto Rico: II. Rate and mechanism of biotite  
848 weathering. *Geochim. Cosmochim. Acta* 62, 227 – 243

849 Newman ACD (1969) Cation exchange properties of micas. I. The relation between mica  
850 composition and potassium exchange in solutions of different pH. *J. Soil. Sci.* 20, 357-  
851 373.

852 Newman ACD, Brown G (1966) Chemical changes during the alteration of micas. *Clay Miner.*  
853 23:337–342

854 Olander D.R., Eyal Y. (1990a) Leaching of uranium and thorium from monazite: II. Elemental  
855 leaching. *Geochim. Cosmochim. Acta* 54, 1879-1887.

856 Paces, T. (1983). Rate Constants of Dissolution Derived from the Measurements of Mass  
857 Balance in Hydrological Catchments. *Geochim Cosmochim Ac* 47, 1855-1863.

858 Pelt, E., Chabaux, F., Innocent, C., Navarre-Sitchler, A.K., Sak, P.B., Brantley, S.L., (2008).  
859 Uranium-thorium chronometry of weathering rinds: Rock alteration rate and paleo-  
860 isotopic record of weathering fluids. *Earth Planet. Sci. Lett.* 276, 98-105.

861 Pelt, E., Chabaux, F., Stille, P., Innocent, C., Ghaleb, B., Girard, M., Guntzer, F., (2013).  
862 Atmospheric dust contribution to the budget of U-series nuclides in soils from the  
863 Mount Cameroon volcano. *Chem. Geol.* 341, 147-157.

864 Rezzoug, S., Fernex, F., Michel, H., Barci-Funel, G., Barci, V., (2009). Behavior of uranium and  
865 thorium isotopes in soils of the Boréon area, Mercantour Massif (S.E. France): Leaching  
866 and weathering rate modeling. *J. Radioanal. Nucl. Chem.* 279, 801-809.

867 Rihs S., Gontier A., Pelt E., Fries D., Turpault M-P. Chabaux F. (2016a) Behavior of U and Th  
868 series nuclides in soils during a land cover change. *Chem. Geol.* 441, 106-123.

869 Rihs, S., Prunier, J., Thien, B., Lemarchand, D., Pierret, M.-C., Chabaux, F., (2011). Using  
870 short-lived nuclides of the U- and Th-series to probe the kinetics of colloid migration in  
871 forested soils. *Geochim. Cosmochim. Acta.* 75, 7707-7724.

872 Rubin, K.H. (2001). Analysis of  $^{232}\text{Th}/^{230}\text{Th}$  in volcanic rocks: a comparison of thermal  
873 ionization mass spectrometry and other methodologies. *Chem. Geol.* 175, 723–750.

874 Schön R., Winkler G., Kutschera W. (2004). A critical review of experimental data for the half-  
875 lives of the uranium isotopes  $^{238}\text{U}$  and  $^{235}\text{U}$ . *Appl. Radiat. Isot.* 60, 263–  
876 273. Schwertmann, U., (1964). Differenzierung der Eisenoxide des Bodens durch  
877 Extraktion mit Ammoniumoxalat-Lösung. *Zeitschrift für Pflanzenernährung, Düngung,*  
878 *Bodenkunde.* 105, 194-202.

879 Seddoh, F.K. (1973). Altération des roches cristallines du Morvan (granite, granophyres,  
880 rhyolites). Etude minéralogique, géochimique et micro-morphologique. Ph. D. Thesis,  
881 Dijon Univ.

882 Sims, K.W.W., Gill, J.B., Dosseto, A., Hoffmann, D.L., Lundstrom, C.C., Williams, R.W., Ball, L.,  
883 Tollstrup, D., Turner, S., Prytulak, J., Glessner, J.J.G., Standish, J.J., Elliott, T., (2008). An  
884 Inter-Laboratory Assessment of the Thorium Isotopic Composition of Synthetic and Rock  
885 Reference Materials. *Geostand. Geoanal. Res.* 32, 65-91.

886 Suresh P., Dosseto A., Hesse P., Handley H. (2013) Soil formation rates determined from  
887 Uranium-series isotope disequilibria in soil profiles from the southeastern Australian  
888 highlands. *Earth Planet. Sci. Lett.* 379, 26-37.

889 Tamm O. (1922) Um best ämning ow de oorganiska komponenterna i markens gelcomplex.  
890 *Medd. Statens Skogsförsökanst.* 19, 385-404.

891 Taboada T., Cortizas A. M., Garcia C. and Garcia-Rodeja E. (2006) Particle-size fractionation  
892 of titanium and zirconium during weathering and pedogenesis of granitic rocks in NW  
893 Spain. *Geoderma* 131, 218–236.

894 Taylor A., Blum J., Lasaga A. (2000a) The dependence of labradorite dissolution and Sr  
895 isotope release rates on solution saturation state *Geochim. Cosmochim. Acta* 64, 2389 –  
896 2400.

897 Taylor A., Blum J., Lasaga A., MacInnis I. (2000b) Kinetics of dissolution and Sr release during  
898 biotite and phlogopite weathering. *Geochim. Cosmochim. Acta* 64, 1191–1208.

899 Taylor, A., Blum, J.D., (1995). Relation between Soil Age and Silicate Weathering Rates  
900 Determined from the Chemical Evolution of a Glacial Chronosequence. *Geology* 23, 979-  
901 982.

902 Turpault M.P, Fichter J., Ezzaïm A., Ranger J. (1998) Quantitative mineralogy of acidic soils.  
903 Congrès mondial de science du sol, 20-26/08, Montpellier, France

904 Turpault M.P. and Trotignon L. (1994) The dissolution of biotite single crystals in dilute HNO<sub>3</sub>  
905 at 24°C: evidence of an anisotropic corrosion process of micas in acidic solutions.  
906 *Geochim Cosmochim Acta* 58, 2761-2775.

907 Vigier N., Bourdon B., Turner S. P. and Allegre C. J. (2001) Erosion timescales derived from U-  
908 decay series measurements in rivers. *Earth Planet. Sci. Lett.* 193, 549-563.

909 Vigier, N., Bourdon, B., (2011). Constraining Rates of Chemical and Physical Erosion Using U-  
910 Series Radionuclides. In: Baskaran, M. (Ed.), *Handbook of Environmental Isotope*  
911 *Geochemistry. Advances in Isotope Geochemistry.* Springer Berlin Heidelberg, pp. 553-  
912 571.

913 Voinot A. (2012) Contribution des isotopes du bore à l'étude des mécanismes et bilans de  
914 l'altération des minéraux des sols Ph. D. Thesis, Strasbourg Univ.

915 Wan J., Tokunaga T. K., Ashby P. D., Kim Y., Voltolini M., Gilbert B. and DePaolo D. J. (2018)  
916 Supercritical CO<sub>2</sub> uptake by nonswelling phyllosilicates. *Proc. Natl. Acad. Sci. U. S. A.*,  
917 115, 873–878

918 White A. F. and Buss H. L. (2014) Natural weathering rates of silicate minerals. In *Treatise on*  
919 *Geochemistry (Second Edition)* (ed. J. I. Drever) vol 7. Elsevier, Oxford, pp. 115–155

920 White A.F. (2002) Determining mineral weathering rates based on solid and solute  
921 weathering gradients and velocities: application to biotite weathering in saprolites.  
922 *Chem. Geol.* 190, 69 – 89.

923 White A.F. and Brantley S.L. (2003) The effect of time on the weathering of silicate minerals:  
924 why do weathering rates differ in the laboratory and field? *Chem. Geol.* 202, 479-506

925 White A.F., Blum A.E., Schulz M.S., Vivit D.V., Stonestrom D.A., Larsen M., Murphy S.F., Eberl  
926 D. (1998) Chemical weathering in a tropical watershed, Luquillo Mountains, Puerto  
927 Rico: I. Long-term versus short-term weathering fluxes. *Geochim. Cosmochim. Acta* 62,  
928 209-226.

929 White A.F., Schulz M.S., Lawrence C.R., Vivit D.V., Stonestrom D.A. (2017). Long-term  
930 flowthrough column experiments and their relevance to natural granitoid weathering  
931 rates. *Geochim Cosmochim Acta* 202, 190-214.

932 Williams, R.W., Collerson, K.D., Gill, J.B., Deniel, C. (1992). High Th/U ratios in subcontinental  
933 lithospheric mantle: mass spectrometric measurement of Th isotopes in Gausberg  
934 lamproites. *Earth and Planet. Sci. Lett.* 111, 257–268.

935

## Figure captions

Fig. 1: Location of the experimental Breuil-Chenué INRA site and of soil profiles developed under the native forest from which biotite grains were extracted. The profiles studied by Rihs, Gontier et al. (2016) under the substituted Oak stand are also reported (short-term weathering rate, see the text for explanation).

Fig. 2: Mass fraction of the remaining parent biotite and weathering products in the study grains without quartz contributions (from Voinot 2012).

Figure 3: Evolution of Th and U contents in the grains relative to the K<sub>2</sub>O contents.

Figure 4: Evolution of U/Th ratios in the grains relative to the fraction of remaining parent biotite (a) or TiO<sub>2</sub> contents (b).

Figure 5: Evolution of (<sup>234</sup>U/<sup>238</sup>U) ratios in the grains relative to the fraction of remaining parent biotite present (quartz excepted, see the text for explanation). (<sup>234</sup>U/<sup>238</sup>U) ratios in the 20-30 cm (> 200 μm) and the saprolite samples are inconsistent with the weathering stage deduced from major elements.

Figure 6: U-series disequilibria measured and modeled from the separated grains. Model 1 and model 2 stand for the two extreme models derived from the range of solutions allowing for a description of the data. Lengths of time required for evolution from the 120-140 cm to the 20-30 cm (50-200 μm) samples are modeled as 6 and 52 ky in models 1 and 2, respectively.

Figure 7: Measured and modeled U (a) and Th (b) isotopic ratios vs (<sup>238</sup>U/<sup>232</sup>Th) ratios in the separated grains. "Model het. U/Th" accounts for a potential initial U/Th heterogeneity and corresponds to a model with a slightly different initial (<sup>238</sup>U/<sup>232</sup>Th) ratio (0.37 instead of 0.48, see the text for explanation). The equiline denotes the radioactive equilibrium.

Figure 8: Sets of Eq. 2 solutions allowing for the reproduction of measured activity ratios. For each set of solutions, ratios between the <sup>238</sup>U, <sup>234</sup>U and <sup>230</sup>Th leaching constants are reported as a function of the length of time required for evolution from least to most weathered sample.

Figure 9: Comparison of measured biotite weathering rates with previously reported experimental and field rates (adapted from White and Brantley, 2003 and references therein; Föllmi et al., 2009; Buss et al., 2008, Dosseto et al., 2014, 2019). The dashed-line represents the power function proposed by White and Brantley (2003). The "land cover change" data corresponds to the biotite weathering rate induced by an experimental substitution of vegetation 35 years ago within the same site as that studied here (Rihs, Gontier et al., 2016). The "field Swiss Alp" data report rates from sedimentary chronosequences of the Rhône and Oberaar Glaciers (Föllmi et al., 2009). The "U-series derived rates" ranges report data derived from U-series weathering rates determinations (Dosseto et al., 2014, 2019).

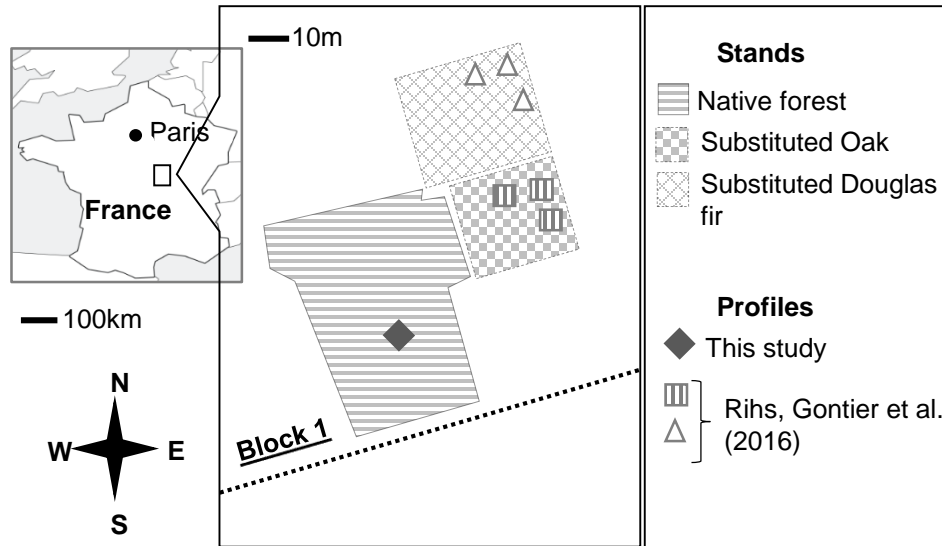


Fig. 1: Location of the experimental Breuil-Chenue INRA site and of soil profiles developed under the native forest from which biotite grains were extracted. The profiles studied by Rihs, Gontier et al. (2016) under the substituted Oak stand are also reported (short-term weathering rate, see the text for explanation).

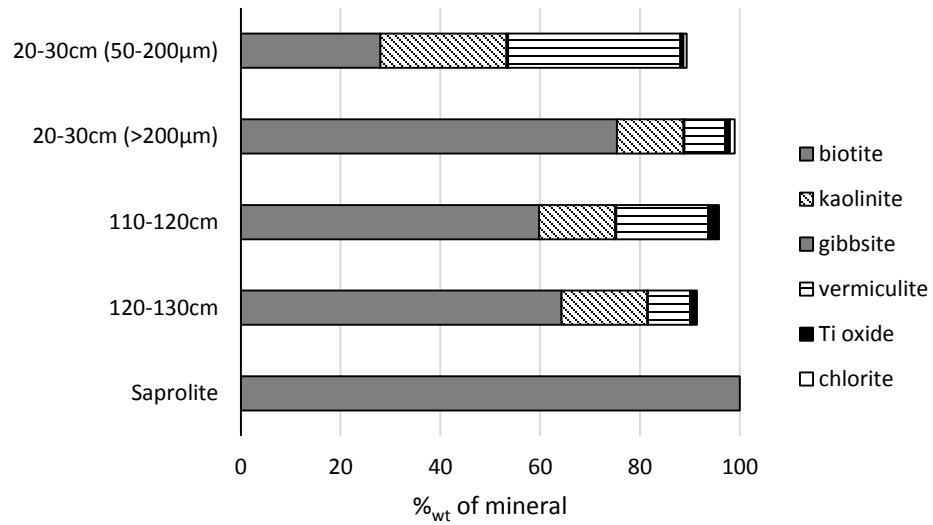


Fig. 2: Mass fraction of the remaining parent biotite and weathering products in the study grains without quartz contributions (from Voinot 2012).

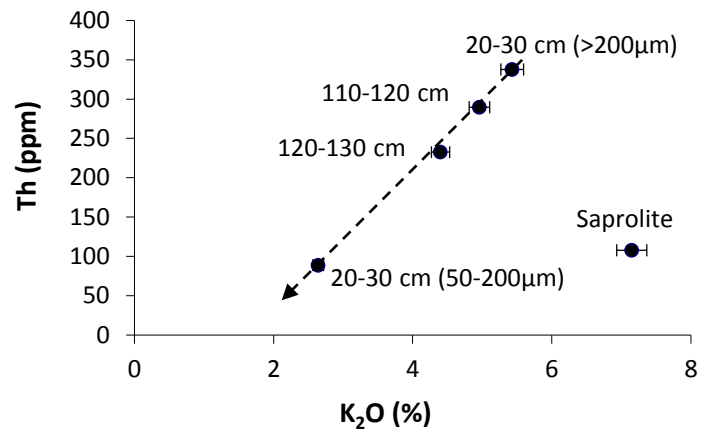
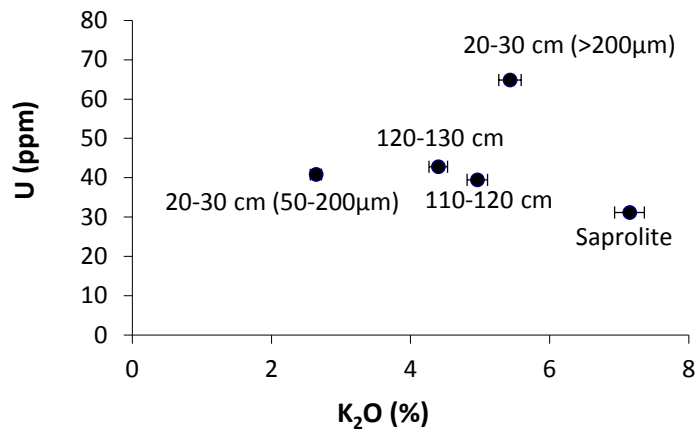


Figure 3 : Evolution of Th and U contents in the grains relative to the K<sub>2</sub>O contents.

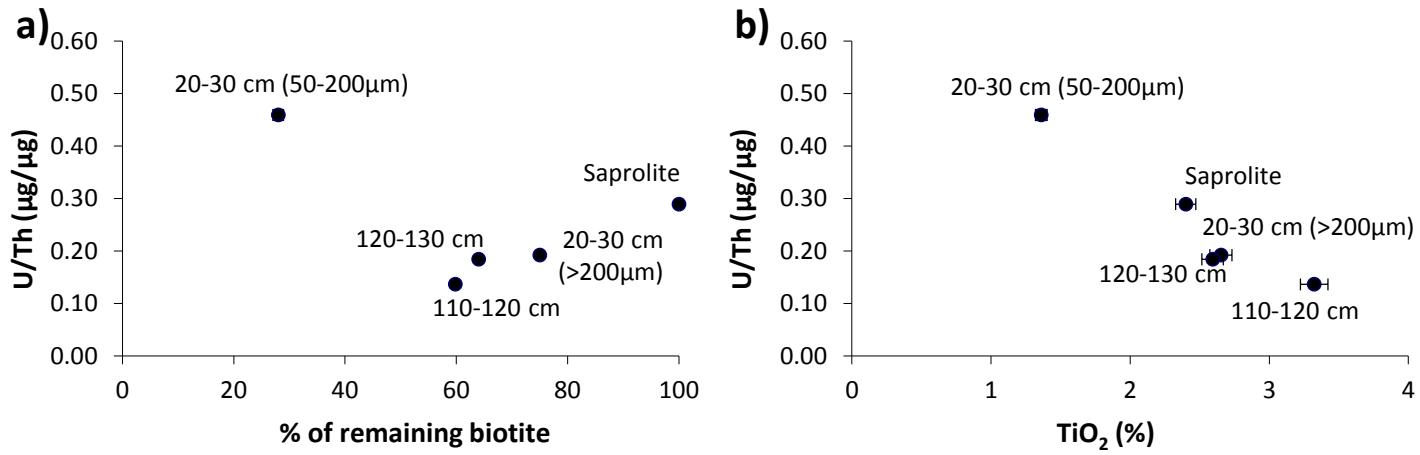


Figure 4: Evolution of U/Th ratios in the grains relative to the fraction of remaining parent biotite (a) or TiO<sub>2</sub> contents (b).

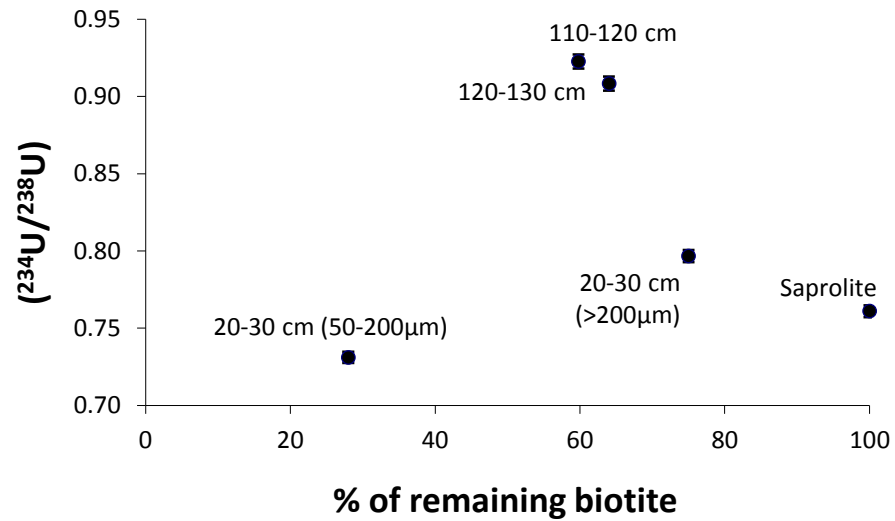


Figure 5: Evolution of  $(^{234}\text{U}/^{238}\text{U})$  ratios in the grains relative to the fraction of remaining parent biotite present (quartz excepted, see the text for explanation).  $(^{234}\text{U}/^{238}\text{U})$  ratios in the 20-30 cm (> 200  $\mu\text{m}$ ) and the saprolite samples are inconsistent with the weathering stage deduced from major elements.

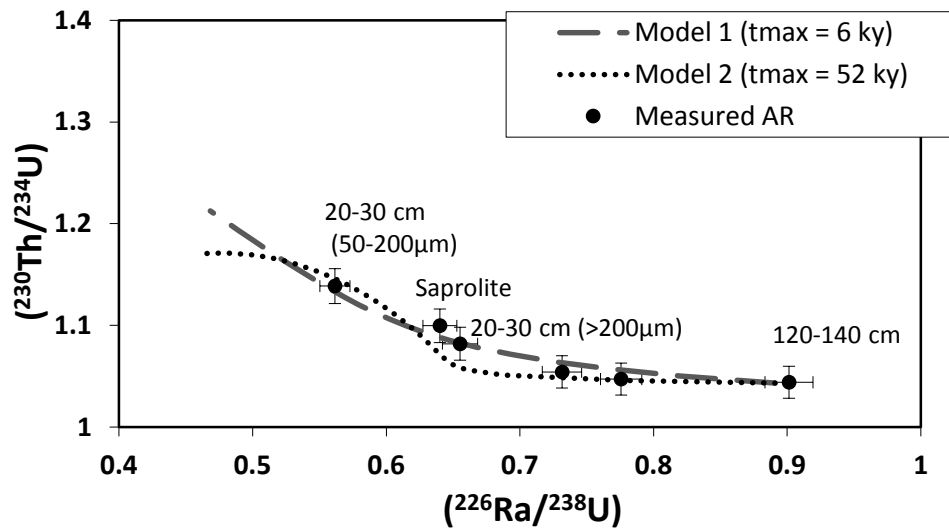
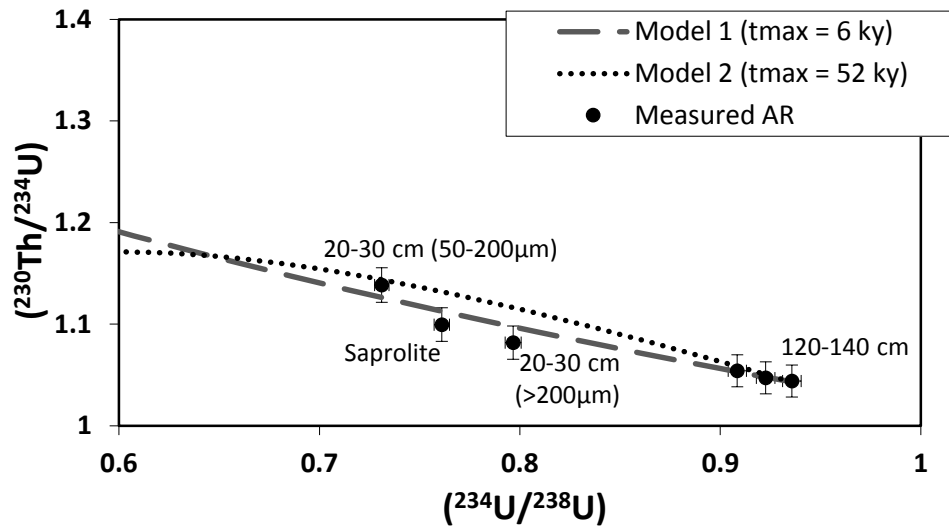


Figure 6: U-series disequilibria measured and modeled from the separated grains. Model 1 and model 2 stand for the two extreme models derived from the range of solutions allowing for a description of the data. Lengths of time required for evolution from the 120-140 cm to the 20-30 cm (50-200  $\mu\text{m}$ ) samples are modeled as 6 and 52 ky in models 1 and 2, respectively.

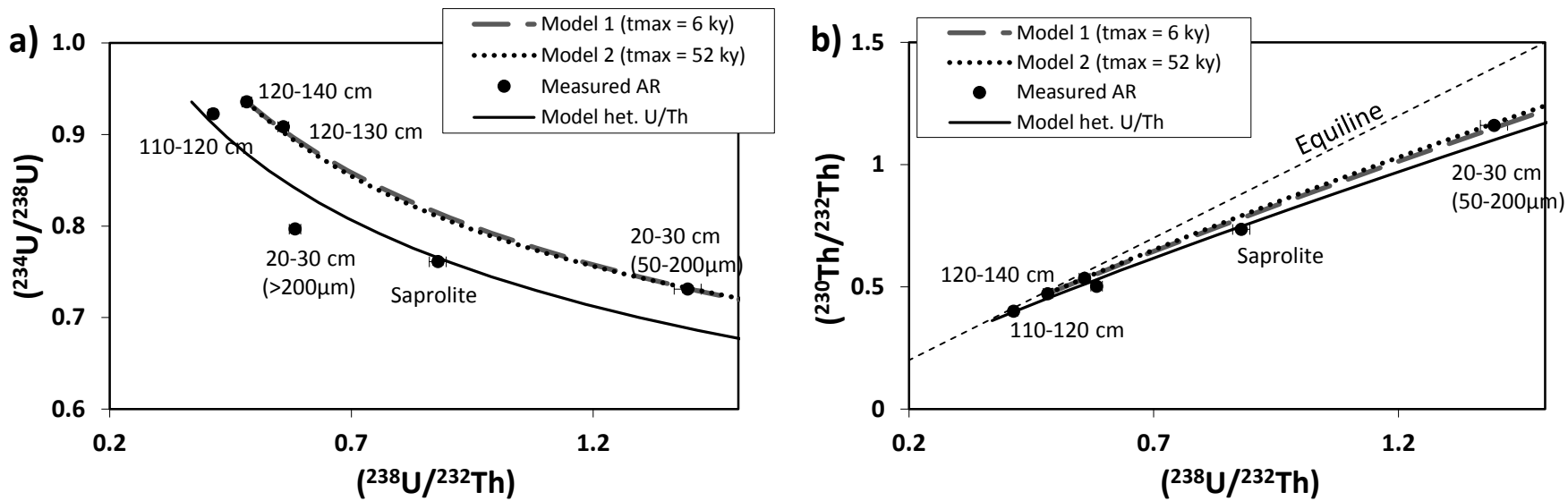


Figure 7: Measured and modeled U (a) and Th (b) isotopic ratios vs  $(^{238}\text{U}/^{232}\text{Th})$  ratios in the separated grains. "Model het. U/Th" accounts for a potential initial U/Th heterogeneity and corresponds to a model with a slightly different initial  $(^{238}\text{U}/^{232}\text{Th})$  ratio (0.37 instead of 0.48, see the text for explanation). The equiline denotes the radioactive equilibrium.

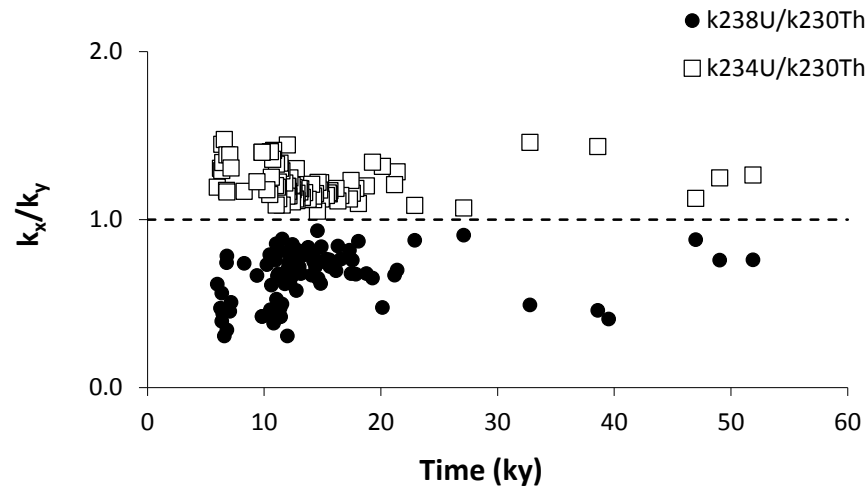


Figure 8: Sets of Eq. 2 solutions allowing for the reproduction of measured activity ratios. For each set of solutions, ratios between the  $^{238}\text{U}$ ,  $^{234}\text{U}$  and  $^{230}\text{Th}$  leaching constants are reported as a function of the length of time required for evolution from least to most weathered sample.

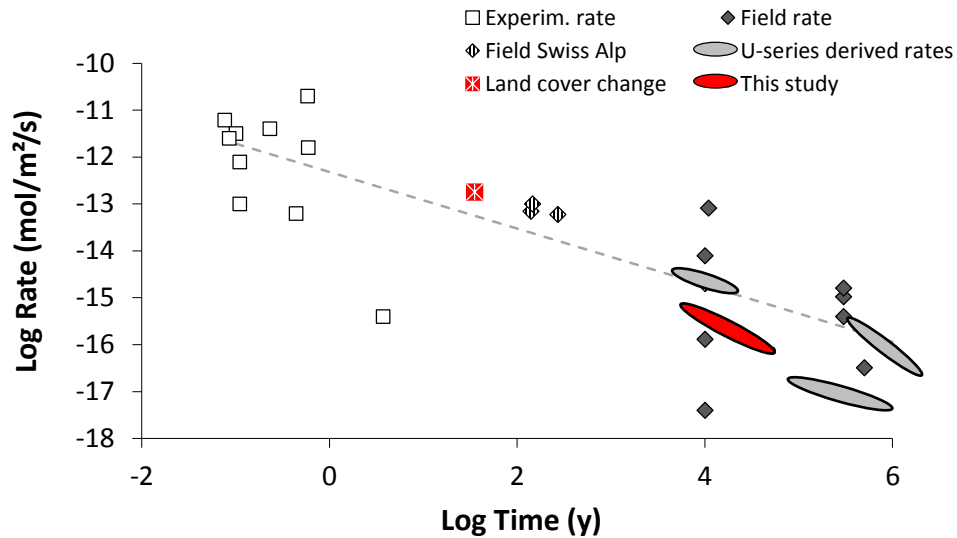


Figure 9: Comparison of measured biotite weathering rates with previously reported experimental and field rates (adapted from White and Brantley, 2003 and references therein; Föllmi et al., 2009; Buss et al., 2008, Dosseto et al., 2014, 2019). The dashed-line represents the power function proposed by White and Brantley (2003). The "land cover change" data corresponds to the biotite weathering rate induced by an experimental substitution of vegetation 35 years ago within the same site as that studied here (Rihs, Gontier et al., 2016). The "field Swiss Alp" data report rates from sedimentary chronosequences of the Rhône and Oberaar Glaciers (Föllmi et al., 2009). The "U-series derived rates" ranges report data derived from U-series weathering rates determinations (Dosseto et al., 2014, 2019).

Table 1: U- and Th-series nuclides concentrations and activity ratios measured in the standard rocks between 2012 and 2014.

Standard/date	[U] μg.g <sup>-1</sup>	[Th] μg.g <sup>-1</sup>	[ <sup>226</sup> Ra] fg.g <sup>-1</sup>	( <sup>234</sup> U/ <sup>238</sup> U)	2SE	( <sup>230</sup> Th/ <sup>232</sup> Th)	2SE	( <sup>230</sup> Th/ <sup>234</sup> U)	( <sup>226</sup> Ra/ <sup>230</sup> Th)	( <sup>238</sup> U/ <sup>232</sup> Th)
<b>BE-N</b>										
01/2012 <sup>b</sup>	2.498 <sup>c</sup>	10.55 <sup>d</sup>	835 <sup>c</sup>	0.996	0.002	0.728	0.003	1.015	0.980	0.721
04/2012 <sup>b</sup>	2.499 <sup>c</sup>	10.59 <sup>d</sup>	nd	0.997	0.003	0.727	0.003	1.015	nd	0.718
10/2012 <sup>b</sup>	2.507 <sup>c</sup>	10.49 <sup>d</sup>	844 <sup>c</sup>	0.998	0.003	0.728	0.004	1.003	0.997	0.727
Mean	2.502	10.54	840	0.997		0.728		1.011	0.988	0.722
2 RSD (%)	0.4	1.0	1.5	0.2		0.2		1.4	2.4	1.3
<b>BCR-2</b>										
05/2013	1.713 <sup>d</sup>	5.902 <sup>d</sup>	573 <sup>c</sup>	1.0009	0.0006	0.883	0.004	0.999	0.992	0.883
05/2013	1.711 <sup>d</sup>	5.890 <sup>d</sup>	574 <sup>c</sup>	1.0001	0.0006	0.885	0.003	1.001	0.993	0.884
12/2013 <sup>a</sup>	1.700 <sup>d</sup>	5.897 <sup>d</sup>	574 <sup>c</sup>	1.0001	0.0006	0.886	0.004	1.010	0.991	0.877
03/2014	1.699 <sup>d</sup>	5.901 <sup>d</sup>	572 <sup>c</sup>	0.9988	0.0007	0.880 <sup>e</sup>	0.003	1.006 <sup>e</sup>	0.993 <sup>e</sup>	0.876
03/2014 <sup>a</sup>	1.690 <sup>d</sup>	5.876 <sup>d</sup>	572 <sup>c</sup>	1.0014	0.0019	0.881 <sup>e</sup>	0.003	1.005 <sup>e</sup>	0.996 <sup>e</sup>	0.875
06/2014	1.702 <sup>d</sup>	5.908 <sup>d</sup>	580 <sup>c</sup>	0.9957	0.0009	0.883 <sup>e</sup>	0.003	1.012 <sup>e</sup>	1.003 <sup>e</sup>	0.877
Mean	1.702	5.896	574	1.000		0.883		1.005	0.995	0.879
2 RSD (%)	1.0	0.4	1.1	0.4		0.5		1.0	0.9	0.9
2SD of relative deviations from the means (%)	0.8	0.6	1.1	0.3		0.4		1.0	1.2	0.9
Analytical uncertainties used in this study (%)	1.0	1.0	1.5	0.5		1.0		1.5	2.0	1.0

2SE are internal standard error from within-run counting statistics. The following radioactive decay constants were used:  $\lambda_{238} = 1.5513 \times 10^{-10} \text{y}^{-1}$  (Jaffey et al., 1971; Schön et al., 2004),  $\lambda_{234} = 2.8263 \times 10^{-6} \text{y}^{-1}$  (Cheng et al., 2000),  $\lambda_{230} = 9.158 \times 10^{-6} \text{y}^{-1}$  (Cheng et al., 2000),  $\lambda_{226} = 4.335 \times 10^{-4} \text{y}^{-1}$  (Holden, 1990) and  $\lambda_{232} = 4.932 \times 10^{-11} \text{y}^{-1}$  (Rubin, 2001).

nd: not determined

<sup>a</sup> mean value published in Ackerer et al. (2016)

<sup>b</sup> mean value published in Claude et al. (2016)

<sup>c</sup> measured with a Thermo- Scientific Triton mass spectrometer (TIMS)

<sup>d</sup> measured with a Thermo- Scientific Neptune multiple collector inductively coupled plasma mass spectrometer (MC-ICP-MS)

<sup>e</sup> corrected from <sup>232</sup>Th peak tailing over <sup>230</sup>Th

Table 2: Major elements contents (in %) in the biotite grains extracted from various soil depths and from the granitic saprolite (after Voinot, 2012)

	LOI 1000°C	SiO <sub>2</sub> (SiO <sub>2</sub> *)	Al <sub>2</sub> O <sub>3</sub> (Al <sub>2</sub> O <sub>3</sub> *)	MgO (MgO*)	CaO (CaO*)	Fe <sub>2</sub> O <sub>3</sub> (Fe <sub>2</sub> O <sub>3</sub> *)	MnO (MnO*)	TiO <sub>2</sub> (TiO <sub>2</sub> *)	Na <sub>2</sub> O (Na <sub>2</sub> O*)	K <sub>2</sub> O (K <sub>2</sub> O*)	$\frac{\text{SiO}_2^*}{\text{Al}_2\text{O}_3^*}$	$\frac{\text{K}_2\text{O}^*}{\text{Al}_2\text{O}_3^*}$
20-30 cm (50-200µm)	11.15	34.8 (29.8)	21.7 (23.4)	5.68 (6.12)	0.07 (0.07)	22.7 (24.5)	0.73 (0.79)	1.36 (1.47)	0.18 (0.19)	2.64 (2.84)	1.27	0.12
20-30 cm (200-2000µm)	6.17	43.5 (34.5)	20.8 (24.1)	4.07 (4.72)	0.06 (0.07)	17.1 (19.8)	0.53 (0.61)	2.65 (3.08)	0.44 (0.51)	5.43 (6.30)	1.43	0.26
110-120 cm	6.41	41.1 (32.2)	19.9 (22.9)	5.45 (6.26)	< dl	18.7 (21.5)	0.47 (0.53)	3.32 (3.82)	0.26 (0.30)	4.96 (5.70)	1.41	0.25
120-130 cm	6.01	44.1 (32.2)	20.2 (24.5)	4.84 (5.87)	< dl	16.1 (19.5)	0.48 (0.59)	2.59 (3.15)	0.31 (0.37)	4.40 (5.34)	1.31	0.22
Saprolite biotite	2.94	43.0 (38.0)	18.9 (20.6)	4.22 (4.59)	0.10 (0.11)	19.0 (20.7)	0.50 (0.54)	2.40 (2.61)	0.70 (0.76)	7.15 (7.78)	1.86	0.38
Saprolite biotite after interlayer extraction (NaCl) <sup>a</sup>	10.33	40.0	15.1	3.40	1.15	15.4	0.44	1.75	6.2	4.05		

Results are given as percent fractions on weight basis after drying at 110°C per gram of extracted grains (quartz included, Voinot, 2012). The values in brackets (\*) refer to the major element contents recalculated per gram of biotite and weathering products without quartz, i.e.; after subtracting quartz contribution to SiO<sub>2</sub> content. The precision is 3%.

LOI 1000°C: Lost on Ignition at 1000 °C.

dl = detection limit (= 0.05 %)

<sup>a</sup> this study

Table 3: U- and Th-series nuclides concentrations and activity ratios in the separated biotite grains.

	[U]	[Th]	( <sup>234</sup> U/ <sup>238</sup> U)	( <sup>230</sup> Th/ <sup>234</sup> U)	( <sup>226</sup> Ra/ <sup>230</sup> Th)	( <sup>230</sup> Th/ <sup>232</sup> Th)	Residual biotite <sup>a</sup>
	μg·g <sup>-1</sup>	μg·g <sup>-1</sup>					%
Uncertainties	± 1 %	± 1 %	± 0.5 %	± 1.5 %	± 2 %	± 1 %	
20-30 cm (50-200μm)	40.8	88.8	0.731	1.139	0.667	1.161	28
20-30 cm (200-2000μm)	64.9	337.6	0.797	1.082	0.752	0.503	75
110-120 cm	39.5	289.6	0.923	1.047	0.794	0.400	60
120-130 cm	42.8	232.6	0.908	1.054	0.756	0.535	64
120-140 cm	49.4	310.2	0.936	1.044	0.913	0.472	nd
Saprolite biotite	31.2	107.7	0.761	1.100	0.757	0.735	100
Saprolite biotite replicate	29.5	96.8	0.762	1.101	0.766	0.776	/

<sup>a</sup>: from Voinot (2012), recalculated without quartz contribution (see the text for explanation).

Table 4: U, Th and Mg (when relevant) recovery during interlayer (1 M NaCl) and amorphous Fe-Al-Mn oxy-hydroxides (0.2 M oxalate acid/ ammonium oxalate) extractions from the saprolite biotite.

	% U	% Th	% Mg
1 <sup>st</sup> extraction interlayer	0.7	0.15	nd
2 <sup>nd</sup> extraction interlayer	0.3	0.02	nd
3 <sup>rd</sup> extraction interlayer	0.05	< dl	nd
Oxy-hydroxides extraction	2	4	0.4

The fractions are relative to the total amount of U, Th and Mg in the mineral. The 3 extractions with 1M NaCl lasted 7 days each and were sequential. The precision of the concentration measurement in the solutions is 10 % for U and Th (ICP-MS analysis) and 3 % for Mg (ICP-AES analysis).

nd: not determined

dl: detection limit

Table 5: Model parameter ranges allowing to fit the measured activity ratios. The leaching constants leading to the minimum and maximum time length are reported (model 1 and 2).

	$k_{238U} (y^{-1})$	$k_{234U} (y^{-1})$	$k_{230Th} (y^{-1})$	$k_{226Ra} (y^{-1})$	$k_{232Th} (y^{-1})$	Time <sup>a</sup>
Range	1.5×10 <sup>-6</sup> - 1.4×10 <sup>-4</sup>	7.6×10 <sup>-6</sup> - 1.5×10 <sup>-4</sup>	3.8×10 <sup>-6</sup> - 1.5×10 <sup>-4</sup>	1.7×10 <sup>-4</sup> - 3.7×10 <sup>-4</sup>	2×10 <sup>-5</sup> - 6×10 <sup>-4</sup>	6-52 ky
Model 1	4.50×10 <sup>-5</sup>	8.71×10 <sup>-5</sup>	7.29×10 <sup>-5</sup>	2.70×10 <sup>-4</sup>	2.24×10 <sup>-4</sup>	6 ky
Model 2	1.89×10 <sup>-5</sup>	2.42×10 <sup>-5</sup>	2.10×10 <sup>-5</sup>	2.30×10 <sup>-4</sup>	3.93×10 <sup>-5</sup>	52 ky

<sup>a</sup>: amount of time required to evolve from the 120-140 cm to the 20-30 cm (< 200 μm) sample